TECHNISCHE UNIVERSITÄT WIEN

A Virtual Clinical Trial on a novel Phantom for Digital Breast Tomosynthesis

DIPLOMA THESIS

submitted in partial fulfillment of the requirements for the degree of

Diplom-Ingenieurin

in

Biomedical Engineering

by

Julia Maria Pospischek, BSc
Registration Number 01525840

to the Faculty of Physics

at the TU Wien

Advisor: Ao.Univ.Prof. Dipl.-Ing. Dr.techn. Martin Gröschl
2nd Advisor: Ao.Univ.Prof. Univ.Doz. Mag. Dr. Wolfgang Birkfellner

Vienna, 12th May, 2022

Julia Maria Pospischek | Martin Gröschl

Technische Universität Wien
A-1040 Wien ▪ Karlsplatz 13 ▪ Tel. +43-1-58801-0 ▪ www.tuwien.at

Erklärung zur Verfassung der Arbeit

Julia Maria Pospischek, BSc

Hiermit erkläre ich, dass ich diese Arbeit selbständig verfasst habe, dass ich die verwendeten Quellen und Hilfsmittel vollständig angegeben habe und dass ich die Stellen der Arbeit – einschließlich Tabellen, Karten und Abbildungen –, die anderen Werken oder dem Internet im Wortlaut oder dem Sinn nach entnommen sind, auf jeden Fall unter Angabe der Quelle als Entlehnung kenntlich gemacht habe.

Wien, 12. Mai 2022

Julia Maria Pospischek

Danksagung

Ich möchte gleich zu Beginn meinen Betreuern danken. Beide standen jederzeit für Fragen und Unklarheiten zur Verfügung und gaben wertvolles Feedback. Danken möchte ich auch DDr. Mag. Johann Hummel und meiner Kollegin Elisabeth für die tolle Unterstützung und die Möglichkeit, an diesem Projekt mitzuarbeiten. Ich kann gar nicht genug für die Unterstützung, die ich von beiden erhalten habe, danke sagen. Abschließend möchte ich mich auch bei meiner Familie, meinen Freunden und meinem Partner bedanken. Ich hätte diese Diplomarbeit sicher nicht fertigstellen können, wenn sie mich nicht immer tatkräftig ermutigt, gerne Korrektur gelesen und meine langen Monologe zu dem spannenden Thema meiner Arbeit gütig ausgehalten hätten. Ohne die finanzielle und emotionale Hilfe meiner Eltern hätte ich nicht meinen Traum vom Studieren in die Realität umsetzen können. Somit bin ich ihnen auf ewig dankbar, dass sie immer an mich geglaubt und mich unterstützt haben.

Acknowledgements

To start with, I would like to thank my supervisors. Both were always available for questions and ambiguities and gave valuable feedback. I would also like to thank DDr. Mag. Johann Hummel and my colleague Elisabeth for their great support and the opportunity to work on this project. I cannot express enough gratitude for the help I received from both of them. Finally, I would also like to thank my family, friends and partner. I would have certainly not been able to finish this thesis, if they had not encouraged me energetically, offered to proofread my work and endured my long monologues on the exciting topic of my work gracefully. Without the financial and emotional help of my parents, I would not have been able to turn my dream of studying at university into reality. Thus, I am forever grateful to them for always believing in and supporting me.

Abstract

For digital breast tomography, an X-ray examination of the human breast to detect cancer, a novel quality assurance phantom was built and shall be investigated in a virtual clinical trial. The local contrast of 20 randomly chosen particles for each of the five size group was found in an image of the calcium carbonate particles spread on a plastic block. The particles were simulated with a verified and tested simulation tool in MATLAB in an image of the plastic alone and the contrast was compared to the original image. As a result, the average difference in contrast of the simulated and the original image for the five size groups range from 0.0043 for the size class 1 to 0.0078 for group 0. The other outcomes are differences in contrast of 0.0055, 0.0056 and 0.006 for the size classes 2, 3 and 4. In conclusion, the virtual clinical trial successfully found a significantly small average difference in contrast of the microcalcifications. The use of this material in the phantom is justified as the exhibited contrast of the original image is satisfyingly similar to the contrast of the simulation. However, the trial was constrained due to the capabilities of the simulation framework and the composition of the original image. In the future tests shall be done on the detectability of the microcalcifications and later on the second type of test objects in the phantom, the non-spiculated mass models.

Kurzfassung

Für die digitale Brusttomographie, eine Röntgenuntersuchung der menschlichen Brust zur Erkennung von Krebs, wurde ein neues Qualitätssicherungsphantom gebaut und soll in einer virtuellen klinischen Studie untersucht werden. Der lokale Kontrast von 20 zufällig ausgewählten Partikeln für jede der fünf Größengruppen wurde in einem Bild der Calciumcarbonat Partikel auf einem Kunststoffblock verteilten gefunden. Die Partikel wurden mit einem verifizierten und getesteten Simulationstool in MATLAB in ein Bild von dem Kunststoff alleine simuliert und der Kontrast mit dem Originalbild verglichen. Infolgedessen reicht der durchschnittliche Kontrastunterschied des simulierten und des Originalbildes für die fünf Größengruppen von 0,0039 für die Größengruppe 1 bis 0,0078 für die Größenklasse 0. Die anderen Ergebnisse sind Kontrastunterschiede von 0,0055, 0,0056 und 0,006 für die Größenklasse 2, 3 und 4. Abschließend fand die virtuelle klinische Studie erfolgreich einen signifikant kleinen durchschnittlichen Unterschied im Kontrast der Mikroverkalkungen. Die Verwendung dieses Materials im Phantom ist gerechtfertigt, da der gezeigte Kontrast des Originalbildes dem Kontrast der Simulation zufriedenstellend ähnlich ist. Der Versuch war jedoch aufgrund der Fähigkeiten des Simulationsframeworks und der Zusammensetzung des Originalbildes eingeschränkt. Zukünftig sollen Tests zur Erkennbarkeit der Mikroverkalkungen und später der zweiten Art von Testobjekten im Phantom, der nicht spikulierten Massenmodelle, durchgeführt werden.

Contents

CHAPTER 1

Introduction

Breast cancer is the second most common type of cancer found in Austria holding 5,918 cases and 1,685 deaths for the year 2020 [1]. Furthermore, 18 percent of all deaths of female cancer patients are caused by this form of tumour, making it the most dangerous for women [2]. In the EU 86,300 deaths due to this malignancy are estimated for the year 2022 [3]. This makes breast cancer hold 13.3% of all cancer diagnoses in the European Union [4]. In the United States 43,250 women are expected to die due to malign tissue of the breast in 2022 [5].

Breast cancer can be found in the human breast concerning male and female patients. However, women are significantly more likely to suffer from this malignancy. The different types of this disease are mostly named after the location of the first occurrence of cancerous tissue before it spreads and turns into an invasive form due to metastasis. This mostly concerns the lymph nodes. Examples are ductal carcinomas starting in the milk ducts and lobular carcinomas forming in the lobules or milk glands (see Figure 1.1) [6] [7] [8].

These carcinomas are also called cancerous lesions. Lesions are abnormal changes in tissue after damage and normally present themselves as lumps. They can be benign or in other terms non-cancerous. The second harmful type of carcinomas is called cancerous or malignant [9] [10]. An important indication of breast cancer is the presence of microcalcifications especially in early stages of the illness. These are calcifications with a diameter smaller than 1 mm and are separated into two types by their material: calcium oxalate and hydroxyapatite. 30% to 50% of all breast cancers are diagnosed due to the presence of microcalcifications in mammograms. It is also suggested that microcalcifications can hint on patient outcomes. Calcium oxalate is primarily found with benign breast lesions and hydroxyapatite with both benign and malignant breast tissue, which makes it the more prominent calcification type. There are two mechanisms, which were found and linked to the appearance of calcifications in the breast's ductal and lobular tissue. The first one includes the accumulation of secretions of mucin in the

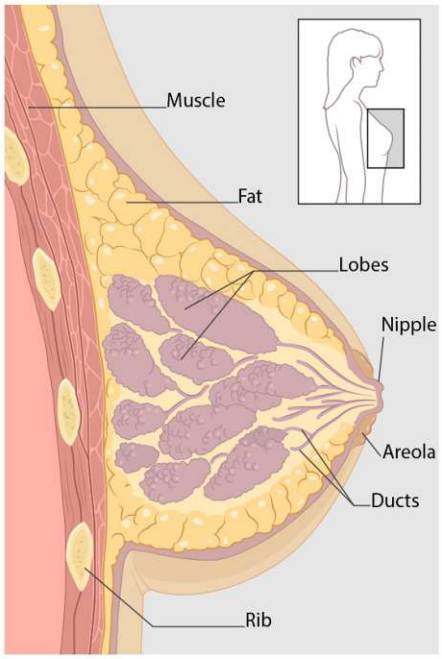

Figure 1.1: A cross-section view of the female breast with the lobes and the ducts. Source: [7]

duct, in parts of the lobules called acinus or in cavities formed by lesions. The second mechanism includes the calcification of endoluminal necrotic material, which consists of cell debris and secretions. Studies suggest that microcalcifications with a size of 0.5 mm and smaller are more prone to hint at malignancy than a size of 1 mm, which is often benign. Moreover, the higher the number of microcalcifications in a volume and the opacity, the higher the chance for malignancy [11] [12].

Risk factors for breast cancer include the family's history with the disease as well as other forms of cancer. Personal characteristics like the body height, the menstrual cycle and the bone mineral density are found to influence the probability to suffer from breast cancer. Other than that, the patient's lifestyle holds an important role along with environmental pollutants. Breast cancer does not show any symptoms at an early stage. At this point it can be most easily treated. This is why screening and early detection are seen as crucial [13]. This is supported by the fact that the death rate of breast cancer declined by 42% due to screening and early detection in the United States of America [14].

Cancer screenings in Austria are managed and financed by the government and include mammography, an imaging technique especially for the human breast using X-rays. The screening program requires the use of digital mammography units, with full-field digital mammography being the most prominent imaging method in clinics [15]. On the other hand, digital breast tomography introduces a pseudo-3-dimensional imaging technique using X-rays and a low dose of radiation, which has been integrated into clinical practice

for more than a decade and has shown promising results [16] especially in denser breasts, where the detection of cancer can be difficult [17].

In order to test the detectability of lesions in digital breast tomography and compare it to the other imaging method called full-field digital mammography in clinics a novel phantom was introduced [16] and improved, resulting in the novel L2 phantom, a next iteration 3D structured breast phantom for tests of detection performance. This phantom consists of a non-static background, microcalcifications and lesion models, which are 3D printed. Especially the implementation of a non-static background makes this phantom stand out amongst other commonly used ones. It should be noted that both human and computerized readers are influenced by the background and might use background characteristics for detection. Hence, the use of plastic spheres in oil having non-fixed positions overcomes limitations of static phantoms, when they are often used by the same readers [18].

The aim of this thesis is to support the evaluation and validation of the novel L2 phantom with a virtual clinical trial. The contrast of the microcalcifications in the phantom shall be investigated with the comparison of the material to simulations done with a simulation tool in order to determine the justification of the potential use of the phantom in quality assurance measurements in the future.

1.1 The physics of mammography

1.1.1 X-rays

X-rays are electromagnetic radiation with a wavelength ranging from 0.01 nm to 10 nm on the electromagnetic spectrum. Electromagnetic radiation can be described with the wave model or with particles called photons. Following the wave model, the wavelength λ_p describes the length of one period of the wave and can be calculated using

$$\lambda_\mathrm{p} = \frac{c_0}{f_\mathrm{p}}, \tag{1.1}$$

whereby f_p is the frequency of the wave and c_0 denotes the wave's speed, which is the speed of light ($2.997{\cdot}10^5$ m/s). The energy of photons E_p is described with the help of Planck's constant h, which is $6.626{\cdot}10^{-34}$ Js, following

$$E_\mathrm{p} = \frac{h \cdot c_0}{\lambda_\mathrm{p}} = f_\mathrm{p} \cdot h \tag{1.2}$$

in the unit electron volt [eV]. It is immanent that the energy is directly proportional to the frequency and inversely proportional to the wavelength. The lower the energy, the lower the frequency and the higher the wavelength. The energy of X-rays is 100 keV to 100 eV.

X-rays are produced with an X-ray tube (see Figure 1.2). The X-ray tube consists of an evacuated tube with a cathode and an anode made of tungsten, molybdenum or rhodium

[19]. The cathode's filament is heated up and electrons are produced with the help of the heat as soon as the thermal energy applied is bigger than the binding energy of the electron e^-. The electrons travel from the negatively charged cathode to the positively charged anode and are accelerated by an applied voltage. The electrons hit the anode and produce electromagnetic waves with the wavelength of X-rays due to the negative acceleration introduced by the electric field of the atoms of the anode. In general, any acceleration of loaded particles results in electromagnetic radiation.

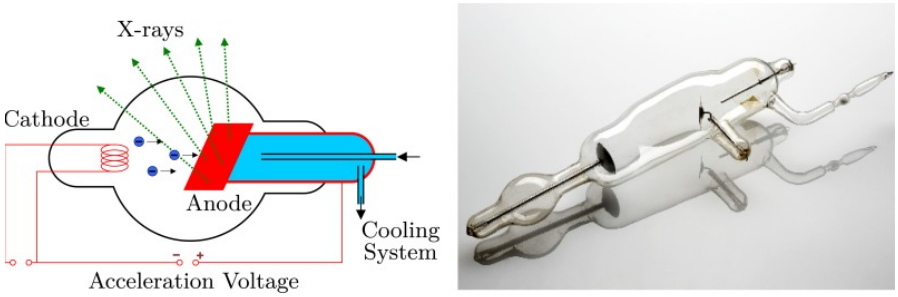

Figure 1.2: A schematic image of a vacuum X-ray tube on the left and a historic realization of the vacuum X-ray tube on the right. In the diagram on the left, the cathode can be found as a coil. Electrons are accelerated towards the anode as blue circles by the acceleration voltage and produce X-rays in green after rapid deceleration at the anode, which is connected to a cooling system. Source: [20]

Two mechanisms are responsible for the production of electromagnetic radiation. The first one happens when the electron loses its kinetic energy due to it interacting with the nucleus of the target. The nucleus forces the electron in a deviated direction with a reduced speed, which means that the electron ends up with less kinetic energy in a changed direction. The difference in kinetic energy forms an X-ray photon. The radiation resulting from this mechanism is called "braking radiation" or "Bremsstrahlung" and exhibits a continuous spectrum, as the loss of kinetic energy can vary from zero to the total energy of the original electron.

The second less common process to cause X-rays results from ionization. The target atom is ionized as the electron from the cathode removes an electron in one of the inner shells of the target atom. An orbital electron from an outer shell travels to the inner shell to substitute for the missing electron and emits an X-ray photon. The energy of the photon is the difference of the binding energy of the two orbital electrons. This results in a discrete spectrum that depends on the material of the target anode and is therefore called characteristic radiation [20]. This spectrum includes sudden high spikes depending on specific photon energy. Together, both effects create a typical X-ray spectrum depending on the material. The continuous spectrum is broad with characteristic spikes on top (see Figure 1.3) [21].

In order to remove low energy radiation, which is also called soft X-rays, X-ray filters are added between the patient and the source. Soft X-rays are non-penetrating and do

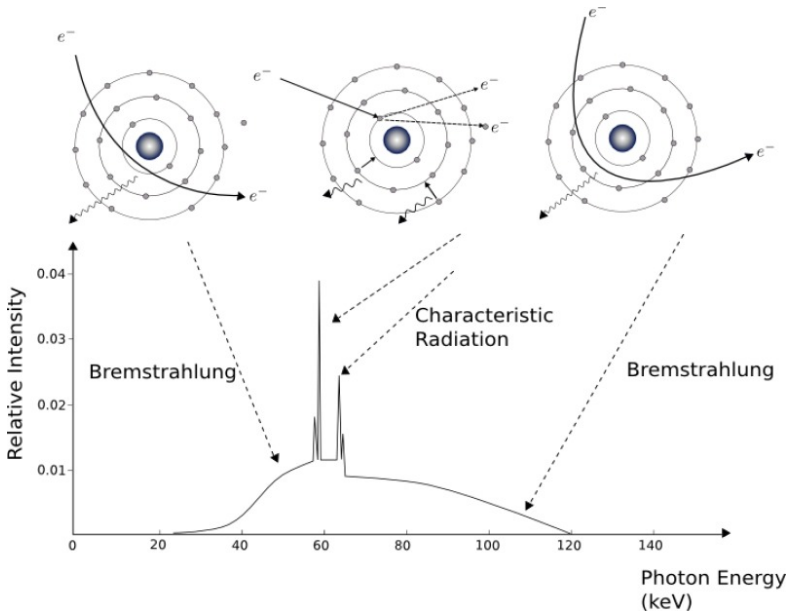

Figure 1.3: An image of an X-ray spectrum with the continuous Bremsstrahlung and the spikes of the characteristic radiation. A diagram of the development of the characteristic radiation is in the middle of the upper three drawings. The approaching electron removes an electron from an inner shell and radiation is emitted as electrons from the outer shells move inwards. The interaction of an electron with a nucleus is described on the upper left and right picture. The electron's course is changed and electromagnetic radiation is emitted as continuous Bremsstrahlung. Source: [20]

not improve the image quality while still increasing the dose of radiation hitting the patient [20]. The most commonly used filter material is aluminium, but the contrast has to be taken into account as it decreases with increasing energy. While the patient dose is reduced by filters, the beam's mean photon energy is increased as the low energy parts of the spectrum are removed. The loading is increased to compensate for the smaller dose at the receptor with an increase in mAs [22, p. 111].

The high energy part of the spectrum is also not desired as it results in low contrast [21]. Examples of used materials for the anode are molybdenum, rhodium, silver and aluminium, which produce characteristic spectra with different maxima in energy [23]. In order to filter radiation above a threshold keV the k-edge filter is used. Radiation above the k-absorption edge is absorbed as the binding energy of the k-shell electrons in the target are exceeded. Hence, the k-edge is the threshold for attenuation, while the attenuation decreases at first with increasing energy and then jumps up again at the k-edge. The binding energy depends on the atomic number Z and therefore the size of the atom. For example, molybdenum is frequently used in mammography due to its k-edge at 20 keV, matching the wanted interval of energy for optimal contrast for the given tissue [24]. The material of the filter depends on the density and size of the breast.

For a denser breast a higher energy would be desired, which is more penetrating. In this case, a filter material with a higher k-edge is selected [21].

X-ray measures the loss of energy caused by the different absorption rates of different materials. A negative image is created of the object showing the difference of absorption with different shades of grey [20]. The absorption of the tissues depends on the radiological density, which is connected to the density and the atomic number of the material, which is equal to the number of protons in the nucleus. X-rays are commonly used to image bones because of the material calcium, which is found in bones and holds a high atomic number that results in high contrast [25]. The term attenuation describes the removal of photons in a beam of rays when it travels through a material [26, p. 44], which is equal to the reduction in intensity of the radiation [20].

As photons travel through matter scattering can occur, which describes the deviation of photons. There are two types of scattering. The first is called Rayleigh scatter, classical scatter or coherent scatter and involves the exciting of the whole atom. This effect is most prominent with low energy rays and is therefore especially seen in mammography. No ionization occurs as no electrons are removed from the atom. The wave hitting the atom causes the electrons to oscillate. The energy produced this way leaves the atom in the form of a photon with the same energy and wavelength as the incident photon but in a deflected direction. This deflected photon is then later falsely detected on the detector causing noise (see Figure 1.4). The occurrence of classical scatter decreases with increased energy.

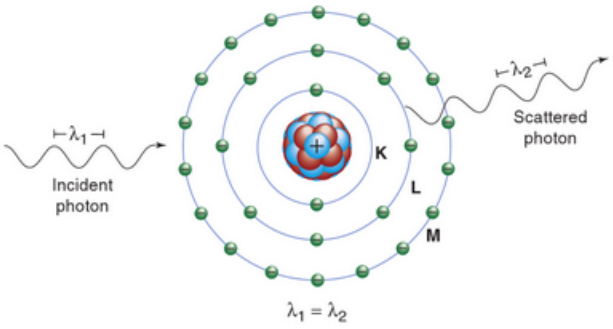

Figure 1.4: A diagram describing Rayleigh scatter. A photon with the wavelength λ_1 hits the atom consisting of the positive nucleus and three electron shells K, L and M. A photon of the same wavelength λ_2 is produced with a changed direction due to the electrons oscillating in the shells. Source: [26, p. 39]

The second type of scatter radiation is called Compton scattering, inelastic or non-classical scattering and is more prominent in soft tissue and when imaging with higher energy X-rays. The photon interacts with an electron from the outer shells of the atom (also called valence electron) and removes it from the atom. The photon is scattered with an angle of deflection (see Figure 1.5). The energy of the original photon, that hits the

atom, is separated into the new photon and the kinetic energy of the omitted electron (now called Compton electron). The energy of the scattered photon depends on the deflection angle and the original energy of the incident photon. The higher the energy of the photon hitting the atom, the lower the energy of the scattered photon and higher the wavelength as more energy is transferred to the Compton e^- [26, pp. 39-41].

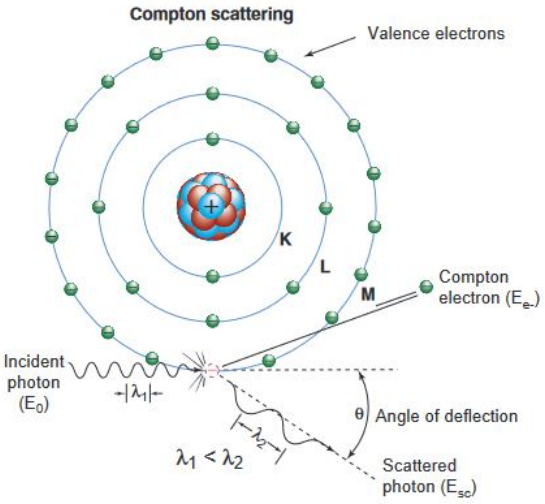

Figure 1.5: A diagram of Compton scatter. An incident photon with high energy and the wavelength λ_1 hits an atom and ionizes it with the removal of a valence electron from one of the outer atom shells (denoted with K, L and M with M being the most outer shell), which turns into a Compton electron. The scattered photon experiences deflection and loses energy to the Compton electron and therefore has a larger wavelength λ_2. Source: [26, p. 40]

One should not forget photoelectric absorption (also called the photoelectric effect) and pair production. The photon's energy needs to exceed 2×511 keV in order for pair production to happen, which is the creation of an electron and a positron when the photon is near an atomic nucleus. Because X-rays do not meet this threshold, pair production is not very prominent in X-ray. The absorption of X-rays follows Lambert-Beer's law

$$I = I_0 \cdot e^{-\mu x}. \tag{1.3}$$

The observed intensity I depends on the original intensity I_0 and the length of the object x together with the attenuation coefficient μ [20]. The photoelectric effect describes the incident photon colliding with an atom and transferring all of its energy to an electron, which is then called a photoelectron and ejected from the atom [27]. High energy photons travel through mater more easily, resulting in less photoelectric interaction. Following this, the probability of photoelectric absorption is equal to $(\frac{Z}{E})^3$ with Z being the atomic number and E the photon energy. In X-ray imaging the photoelectric effect and Compton scatter are mostly prominent in comparison to Raleigh scatter and pair production [28].

The linear attenuation coefficient μ is a material specific constant that includes all possible interactions a photon can have with matter and is given in cm^{-1}. μ can be found through the fraction of the removed photons of a mono-energetic beam per unit thickness or the sum of the linear attenuation coefficients of each interaction following

$$\mu = \mu_{\text{Rayleigh}} + \mu_{\text{Compton}} + \mu_{\text{pair production}} + \mu_{\text{photoelectric}}, \tag{1.4}$$

with the attenuation coefficient for Rayleigh and Compton scatter as well as the photo-electric effect and pair production [27] [29]. The attenuation coefficient also coincides with the product of the number of atoms per unit volume and the interaction cross-section per atom. The number of atoms depends on the atomic number and the density of the material and is the reason why μ is increased with an increased atomic number and density.

The mass attenuation coefficient is found using the dependence of the linear attenuation coefficient on the density. The density on the other hand is highly dependent on the physical state of the material, which makes the linear attenuation coefficient insufficient for data comparison. The mass attenuation coefficient is the fraction of the linear attenuation coefficient and the density $\frac{\mu}{\sigma}$ and has the unit m^2/kg. Historically, the dimensions cm^2/g have been used in the past [22, pp. 24-25].

In order to improve image quality and subsequently decrease the influence of scatter anti-scatter grids are applied. These are lead strips, which are most commonly made with aluminium and carbon fibre in between, because carbon fibres have a low attenuation. The grid absorbs scatter radiation while letting the wanted primary radiation through. The spaces between the strips are aligned with the path of the primary radiation and the scattered radiation is absorbed as its path hits the lead strips. However, a small portion of the primary radiation is absorbed. Hence, the usage of a grid requires higher mAs and subsequently more dose. Still, the increase in quality and decrease in scatter is seen as favourable over an increased dose [30]. Grid-line artefacts can also result from the use of an anti-scatter grid. These can be avoided by oscillating the grid, but do not help in case of a very short duration of the exposure or slow oscillation [26, p. 256].

The Bucky factor B_f gives the influence of the grid on the total signal and is defined as

$$B_f = \frac{P^- + S^- + G^-}{P^+ + S^+ + G^+}, \tag{1.5}$$

with P being the primary radiation, G the glare and S the scattered radiation. The minus stands for the absence of a grid and the plus for its use. The glare is scatter of the signal at the detector while S happens due to the patient to be imaged. G depends on the detector geometry and the material. As G only happens after the anti-scatter grid, it is hard to distinguish it from S. B_f is a measure of the needed increase in dose in order to keep the power of the signal constant when using a grid. As different grids are used for different manufacturers and mammography units, the scatter-to-primary ratio (SPR) can be found experimentally for geometries. It is the fraction of the scattered radiation

to the primary radiation. It should be noted that no grids are applied in tomographic 3D imaging like DBT [31]. This is due to the increase in dose, which is needed with a grid, and the problems that come from the moving detector and source geometry, which would force the grid to move with them [32].

Another factor influencing image quality is beam hardening. As the patient absorbs lower energy radiation and only high energy photons are able to travel through the body and hit the detector, the average energy at the detector is higher than the beam's energy before it hits the patient. The average X-ray energy is increased as fewer and high energy photons hit the detector. The low energy X-rays are attenuated more than high energy rays, removing the lower energies from the spectrum. The contrast is decreased due to this effect because it was stated before that contrast is high for low energy [28] [33]. Artefacts may occur due to beam hardening and are seen as increased brightness in the image as high energy photons hit the screen. However, these artefacts are very rare [34].

The part of the X-ray spectrum with lower energy results from supplying the tube with little kV and improves the contrast but also increases the dose as more energy is absorbed by the patient, less radiation is able to travel through the body and the beam is hardened more. Hence, mAs might be increased to produce more radiation. Contrast is also important to consider when the patient is thicker. The ability of the electromagnetic radiation to penetrate decreases with increasing thickness, while the dose increases. Hence, more kV are used for thicker objects with a worsened contrast [28].

The quality of the image and the dose the patient experiences is subject to the product of the tube current and the exposure time with the unit mAs, as well as the filtration applied and the tube voltage or potential in kVp (kilo peak voltage) [35]. The tube voltage is applied symmetrically to the tube, with the anode and cathode experiencing half the voltage with opposite directions. The current is applied to the cathode's filament to heat it up [22, p. 103]. The filament current affects the number of electrons removed from the cathode and subsequently the number of photons, while the tube current affects the energy and the number of photons. The tube voltage is able to alter the average and maximum energy of the spectrum, as well as the characteristics of the spectrum resulting from Bremsstrahlung. Characteristic radiation only takes place at higher tube potentials and photon energy [36] [28].The absorbed dose describes the energy deposited in a body and is measured in Jkg^{-1} [37]. The dose should be as small as reasonably possible when looking at the contrast, as breast cancer produces small lesions, which require high detail. Moreover, a higher exposure time altering the mAs configurations results in motion blur as the patient is more likely to start moving [21].

1.1.2 Mammography

Breast cancer screening aims to detect the illness as early as possible with higher chance of better treatment, while profiting from the low costs and low dose with good image quality that are associated with mammography. In mammography imaging three types of masses are of interest: microcalcifications, irregular masses (also called spiculated

when having spicules or non-spiculated when having a round shape) and distortions of breast tissue. In both mammography screening to detect breast cancer or diagnostic mammography looking for and diagnosing already detected distortions, the fact that cancerous and healthy glandular tissue have similar attenuation coefficients has to be considered. Moreover, this difference is larger for low energy levels and increases with decreasing energy. Because of this, X-rays with low energy in the range of 15 to 30 keV are used in mammography, with mammography units being built to only examine the breast. Due to the low energy spectrum used in mammography to achieve the best contrast with bigger difference in attenuation, the dose is increased and the spatial resolution of the detector has to be great while it has to be compatible with high doses to begin with. This trade-off of detectability and dose is the reason, why there are strict quality measures applied in mammography.

A schematic image of a mammography system can be found in Figure 1.6. When looking at the mammography system, the X-ray tube is similar to imaging units for other parts of the body. However, mammography units use an automatic exposure control to find the correct mAs value for the chosen kVp. This is done with a feedback circuit. The current is a function of kV and adjusted accordingly together with the filter material based on a test exposure. The port of the tube where the photons leave is made of beryllium with a low atomic number. This way, high energy X-rays are filtered. The tube filtration after the port uses materials with a k-edge of 20 to 27 keV in order to remove the high energy part of the spectrum as well as the low energy parts that result in a high dose for the patient. The collimator is used for collimation or restriction of the X-ray beam. This is needed in order to ensure that the central axis of the X-ray beam is perpendicular to the detector. This results in less unwanted dose in the area of the lungs and upper body, when only the breast should be imaged.

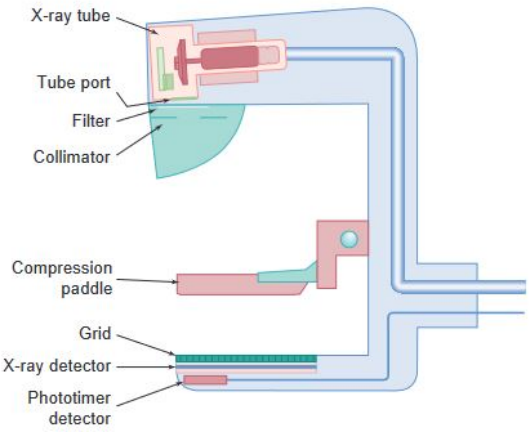

Figure 1.6: A schematic drawing of a mammography unit and its parts. Source: [26, p. 240]

The patient is positioned between the X-ray source and the detector, with the breast

being compressed using the compression paddle. The breast thickness is decreased and the patient is less likely to move. The decreased thickness results in less dose needed and less scatter. Furthermore, overlapping tissue is reduced, which is the most prominent cause of bad detectability of lesions in 2D mammography. Although the compression of the breast decreases scatter, anti-scatter grids are still used on top of the detector. The thin plates are made of copper and absorb secondary radiation that results from scatter while oscillating to avoid artefacts. The use of grids gives a Bucky factor between 2 and 3, which means that double or triple of the dose is needed. Still, the image contrast can be improved by around 40% with these grids.

After the grid the detector of the mammography unit can be found. Screen-film detectors used in mammography are composed of a screen, a light-sensitive emulsion film and a cassette. The cassette is made of a material with low attenuation like carbon fibre and the screen is made of phosphor most of the time. The phosphor screen converts X-ray into visible light with a scintillator, which is then detected by the film and the emulsion on top of it. The emulsion on the film faces down against the screen, which faces upwards. The film holds an emulsion of silver halide crystals in gelatin. These grains are sensitized based on the number of photons, that were not attenuated by the patient. The image is then processed with developing the latent image from the exposed film emulsion. The film comes in contact with a liquid developer. The light sensitive silver ions (also called silver halide) are darkened to metallic silver. This is the reason why the exposed areas are dark on a mammogram [26, pp. 238-260]. The image is fixated with a fixer solution, washed with water and dried. Behind the cassette holding the film and screen lies an automatic exposure control device, which alters the exposure by sampling the X-ray beams and counteracts tube overload or damage to the X-ray anode due to thickness of the breast or wrong inputs [38]. The image is then displayed for the physician and the patient with a light view box [39].

Mammography is used in breast cancer screening due to its ability to detect carcinomas, which are found with the help of microcalcifications among other indications and lesions. This ability is significantly high, with between 85 and 90 percent of breast cancer cases being found. However, the success depends on the breast density. The density can be classified in four categories following the guidelines of ACR, with ACR 4 being the thickest and ACR 1 the thinnest with a high percentage of fat tissue and less glandular tissue [40]. The breast consists of three types of tissue: glandular, fibrous (connective) and adipose (fat) tissue. The percentage of these three components in the breast changes with age and is highly individual. With an increasing age, the amount of adipose tissue increases as well. This is important to take into consideration regarding the X-ray attenuation properties of these tissue types. Connective and glandular tissue is seen as radio-opaque or white in the mammogram with a high attenuation and fat tissue as darker or radio-lucent. A denser breast with more glandular tissue absorbs more radiation. Regarding high density microcalcifications are easier to detect than lesions. Lesions have a lower contrast, which makes them hard to detect in denser breasts. The low contrast is a result of the lesion and the breast tissue having similar densities and attenuation characteristics [41]. Thus,

with decreased density, the size of detectable lesions and detectability increases. Less dense breasts include more homogeneous fat tissue, which makes the detectable size of lesions smaller. However, the chance of cancer to develop increases with density [42].

With the density being an important factor influencing detectability, the volumetric breast density (VBD) of a mammogram can be assessed with machine learning algorithms and image processing. The volumetric breast density is the ratio between fibroglandular tissue and the whole volume of the breast [43] and is depicted in a density map showing the local density for each pixel in percentage. The program finds the lowest intensity in the breast image and then calculates the density of the other intensities. Additionally, metadata concerning the imaging system and the applied voltage and current are considered and influence the calculation. With density maps the breast density of patients can be compared [44] and a measure for the probability of masking can be given. The denser the breast is, the more fibroglandular tissue is present, which is a term for the connective tissue and the glandular functional tissue excluding fat tissue [45]. Subsequently, the change of masking is higher, which stands for a decrease in detectability of lesions due to overlapping tissue. The maps are found with the pixel intensity, which is linked to the thickness of the tissue (see Figure 1.7). The advantage of density maps is the fact that it is a quantitative measure of density and hence the risk of suffering from undetected cancer is reduced. In clinics the radiologist rates breast density, which is highly subjective [46].

While the first imaging method designed for mammography included the use of screen-film, the current standard is the use of digital mammography with computer-assisted detection of lesions or 3D imaging techniques like DBT.

Full-field digital mammography (FFDM) holds many advantages in comparison to screen-film mammography. With digital hospital records and storing system, digital mammograms can be accessed, evaluated and taken faster and more conveniently. Patient waiting time can be improved as well as the contrast. The latter is improved due to a larger dynamic range of digital flat panels. This means that in conventional mammography under- and overexposed areas are more common, differences in attenuation are displayed in harsh differences in grey values. The film is only able to register a short interval of attenuation, while the digital detectors have larger exposure latitude registering low and higher exposures with an appropriate response in grey values. In FFDM two images are produced: for processing and for presentation. The raw image "for processing" shows little contrast and all the raw exposure data. The "for presentation" image is processed and the wide dynamic range is altered to meet the requirements of the individual breast. This process is called windowing and stands for only showing a fraction of the measured grey values and improving contrast this way [26, pp. 263-268]. Windowing leads to better image quality for patients under the age of 50, women in their perimenopausal or premenopausal phase and patients with dense breasts as the breast includes three different tissues with specific attenuation behaviour and therefore grey values [47]. Other processing methods can be applied to the image, whose brightness and contrast is no longer defined by the time-consuming chemical processing of the film of

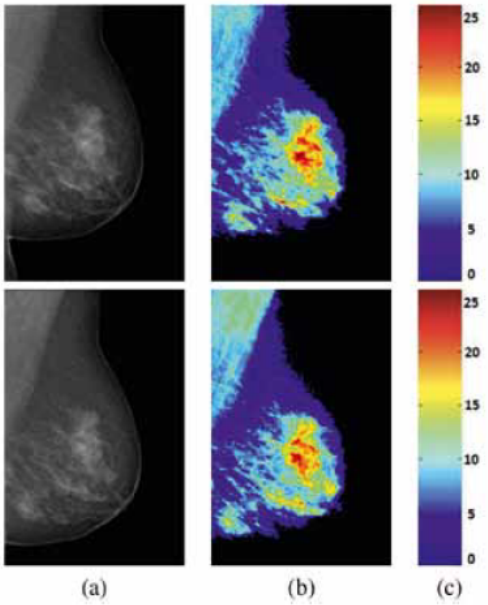

Figure 1.7: The density maps of two breasts. In column (a) two mammograms can be found and in column (b) the density maps with the colour blue showing less dense tissue and the color red annotating the densest areas with the legend in column (c) depicting the colour scale for mm of glandular tissue corresponding to thickness. Source: [44]

classic screen-film mammography. Examples of commonly used methods are measurement and annotation tools and post-processing like frequency processing to achieve a sharper image. Windowing can also be based on different automatic calculations to find the perfect range of grey values. The fact that post-processing can be done to the digital image is seen as one of the biggest advantages of FFDM, as the image on the film of screen-film mammography is fixed once it is chemically processed and cannot be changed. Moreover, the fact that the film is used in acquisition, while displaying the image and then storing marks another disadvantage of screen-film mammography units. In FFDM this is countered with enhancing the imaging process into multiple steps which are done by separate components. The first one is the actual data acquisition using a digital detector. Then the analogue signal is conversed to a digital signal, which is processed and later displayed and stored digitally utilizing a picture archiving and communications system (PACS). Besides that, image processing and reconstruction algorithms for 3D imaging techniques can be applied to digital images easily. Moreover, computer-aided detection of lesions is highly beneficial to improve detection rates of breast lesions. Additionally, the detective quantum efficiency (DQE) is higher in FFDM. The DQE is the fraction of the signal-to-noise ratio (SNR) of the output image to the SNR at the detector. It gives a quantitative measure of how well the imaging system can depict the original signal [39]. After naming the advantages of digital mammography, it should be noted that some smaller clinics still use conventional screen-film detectors. In most cases, they are not

able to transition to digital mammography due to the costs or the needed infrastructure [26, p. 209].

Digital mammography mostly uses the technology of flat panel detector arrays. One flat panel array consists of detector elements lying on a silicon substrate. For each detector element an electronic switch is connected to a storage capacitor and a charge collection electrode. Gate and drain lines are wired horizontally and vertically over the matrix. The transistor is controlled by the gate line and is turned on after image acquisition. The drain lines read out the locally stored charge for each activated line, the signal is amplified, digitized and forms the digital image matrix [26, pp. 264-267]. There is the indirect X-ray conversion TFT (thin film transistor) flat panel array receptor, which uses phosphor emitting light when triggered by X-rays, which is then measured by photodiodes in the detector elements. The transistor switches in the detector elements are activated to read out the signal. The control lines active the switches per row, the read-out lines detect the signal [48]. 12-14 bits are used for the analogue-to-digital conversion. This means that a distinction between 2^{14} grey values and subsequently a favourable resolution can be achieved. In order to display the image, the digital output of the conversion is then again transformed into an analogue image [39].

In Austria, only digital mammography is allowed to be used in breast cancer screening due to the low radiation used with the increased detectability compared to screen-film mammography [15]. However, the resolution of FFDM depends on the pixel size. The smaller the detector parts, the smaller the details shown [26, p. 267]. This pixel size is determined by the transistor switch and the diode included in them. This is why the pixel size cannot be infinitely small. In addition, ghosting is reported in digital mammography detectors, where the preceding signal causes a false increase in output for the following acquisition [48].

1.1.3 Digital breast tomography

Digital breast tomosynthesis or in short DBT is a physical imaging method to screen for and detect breast cancer. It is an enhancement of the conventional mammography producing a pseudo-3-dimensional image [49]. DBT is able to produce this image because of a combination of multiple low-dose images called projections taken at varying angles as the radiation source moves around the breast. The main concern regarding 2D mammography is the overlay of dense tissue. Tumours and lesions can be either masked by overlapping tissue and not be detected or mimicked by artefacts, leading to falsely diagnosed lesions and unneeded further medical and radiological examinations because the 3D anatomy of the breast is captured with a 2D image [50]. Using DBT the physician can look at cross-sectional images of the breast called planes parallel to the detector after reconstruction [51]. The lower rates of false positive diagnoses (diagnosing a signal that is not present) and of false negatives (not diagnosing a signal that is present) [52] are also reflected in studies that have shown that DBT results in a better detection of cancer when used solely or together with FFDM. Yet the latter is still the standard for breast cancer screening [16]. When comparing FFDM units to DBT imaging units, the

detector readout rate for DBT units has to be higher to minimize acquisition time and the X-ray source is able to rotate around the patient. Furthermore, due to the projection images being taken at a fast speed, the detector needs to be modified to reduce ghosting artefacts. Grids are not used in DBT because of the resulting reduction of the already low dose and the need to move the grid together with the X-ray source [53].

In order to reconstruct the projection images into a 3D image of the breast, the locations of the projections are used to compute the vertical position of the tissues. Due to this, the spatial resolution is high for the plane parallel to the detector and worse for the perpendicular direction [53]. Three reconstruction algorithms are known: back-projection (BP) and the filtered back-projection (FBP) algorithm as well as the iterative algorithm. Sometimes combinations of these categories of reconstruction methods are used. FBP describes the use of BP after a filter is applied to the projections, which has significant influence on the result [54]. BP is a "shift-and-add" algorithm, which takes the imaging geometry into consideration. The projections are shifted to match the angle they are taken at and added together. Then the features of one plane are enhanced while the other planes are blurred. The voxel values of the reconstructed result are a sum of the projection pixels at the in-plane positions [55]. This gives a grey value based on all pixel values assessed by the X-rays travelling through the voxel. The filter kernels applied to the projections are used in order to increase sharpness and reduce blurring in the planes [56] [57].

The iterative algorithm on the other hand does not reconstruct in one step. As the name implies, the object model is constantly updated during iterations in order to optimize the object function. The maximum likelihood method is the most commonly used machine learning algorithm using the likelihood function as the objective function. This way the final object model is returned that maximizes the probability of finding the projection [55] thanks to the feedback loop incorporated with the comparison of the calculated projections based on the preceding iteration with the acquisition [58]. Still, the number of iterations needed to report satisfactory results for clinicians is a concern. The higher the number of iterations, the better the model and the better the results. But each iteration is costly in terms of time and computational power [54].

There are specific artefacts in DBT mostly resulting from the reconstruction process. One artefact is called the out-of-plane artefact. It is seen in highly attenuating objects, which are copied to every slice except for the plane they are originally in. Because of the high attenuation, they are not blurred in the other slices and appear even in the out-of-plane ones. As this artefact is highly significant in clinical settings, there are reduction techniques applied by manufacturers to remove these objects before reconstruction. Metal artefacts are similar as metal has a high attenuation and reduces the photons on the detector to a minimum. Hence, little to no signal is detected for the areas in question. Again, due to the analysis of voxels and finding outliers, these artefacts can be removed. Besides, further artefacts like motion artefacts due to the patient moving are seen as blurred areas and hyper- and hypoattenuation caused by a defect or wrongly calibrated detector or debris are reported. In dense breasts, the automatic exposure control forces

the use of high voltage settings. Because of this, the skin is over-penetrated and not imaged properly. These artefacts are called skin-processing error artefacts. Lastly, lesions or calcifications of a significantly small size may not be displayed properly when they lie in between two planes and go out of focus when changing the plane or they are too small and their pixel values are averaged by post-processing [34].

1.2 Contrast quality assessment in DBT and FFDM

1.2.1 Image quality measures

The image contrast depicts the differences in grey scale values and how well materials are represented by distinct grey scale values. In order to see more details and objects in an image, a high contrast and fast transitions between grey scale values are wanted. X-ray images result from the dissimilar characteristics of tissue types and their absorption of radiation [26, pp. 15-16]. The contrast is defined as the ratio of the average signal to the difference in signal when a feature is present. This ratio is based on the fact that small changes in signal are neglectable when the original signal is large. The opposite is the case when the average signal is small. Then small differences are more visible. In general, a high contrast is wanted in medical imaging. This way information is not lost and disease features are detectable. There are mainly two definitions of contrasts used in medical imaging: the local Weber contrast for small features on a uniform and large background and the Michelson or modulation contrast used for patterns. The decision, which definition is used to measure the contrast depends on the image, the features present and the application. The local contrast is mostly used in observer experiments, when a small object shall be identified in a uniform background. The local contrast C is defined as

$$C = \frac{f_\mathrm{f} - f_\mathrm{b}}{f_\mathrm{b}}, \tag{1.6}$$

with $\mathrm{f_f}$ being the signal of the feature and $\mathrm{f_b}$ the signal of the background. The modulation contrast $\mathrm{C_M}$ is defined as

$$C_\mathrm{M} = \frac{f_\mathrm{max} - f_\mathrm{min}}{f_\mathrm{max} + f_\mathrm{min}}, \tag{1.7}$$

with $\mathrm{f_{max}}$ and $\mathrm{f_{min}}$ standing for the highest and lowest signal of an image [22, pp. 63-64].

For the contrast of the displayed image on a computer monitor, a look-up table is needed in order to decrease the bit depth of an image to meet the possible shades of grey that can be shown on a monitor. One example of a look-up table that is most commonly used is the window/level function. It is a non-linear look-up table and sets the grey values below an interval to black and above to white. An example of this method can be found in Figure 1.8. The window W and the level L define the interval $\mathrm{P_1}$ to $\mathrm{P_2}$, where the grey values are depicted. $\mathrm{P_1}$ is equal to $L - \frac{W}{2}$, $\mathrm{P_2}$ is calculated with $L + \frac{W}{2}$. This method of windowing is used by physicians to alter the interval of depicted grey values according to the tissue and patient [26, pp. 89-90].

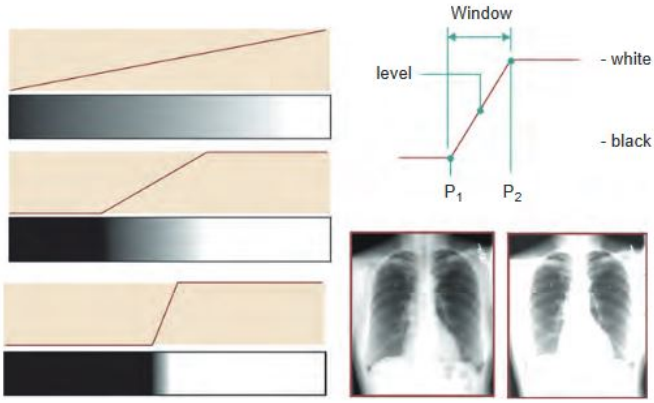

Figure 1.8: An image of the principle of the look-up table window/level. The whole spectrum of grey values in the first diagram on the left side is encoded to two different window/level settings. The window and the level define the interval P_1 to P_2 seen in the upper right drawing, in which the grey values are distinguished. The interval in the middle of the left column is wider than the spectrum of grey values in the bottom left corner. The X-ray image of the chest on the right side is perceived with more white pixels, as the window is narrower and more values are depicted as white. Source: [26, p. 90]

Besides image contrast, there is also subject contrast. It is the change in the X-ray spectrum and intensity resulting from the patient who is imaged. Because of attenuation the profile of the X-ray beam is altered. This contrast can theoretically not be measured because the detector alters the registered contrast. The subject contrast depends on the patient and their tissue with their metabolic and anatomical properties. For example, a lesion may be denser and metabolically more active, changing the subject object. In contrast imaging done with computer tomography or magnetic resonance imaging the subject contrast is improved using contrast agents [26, pp. 87-88].

Mathematical functions can be used to describe image quality in a quantitative manner. Examples include the signal-difference-to-noise ratio (SDNR), the signal-to-noise ratio (SNR) and contrast-to-noise ratio (CNR). The SDNR gives the difference between the pixel values of a target and the background divided by the root-mean-spared background noise. The background noise is the difference between the standard deviations of the background and the feature and squared, divided by two and taken the root of [59]. This way, the SDNR stands for the contrast depending on the noise of the image [60]. The CNR gives a quantitative value of the signal of a feature when noise is present. This signal depends on the size of the object. It is calculated applying the fraction of the contrast and the background noise, while the contrast is found as the difference in mean grey values of the target and the background. Hence, the CNR should only be applied to homogeneous features where the mean pixel value is present in the whole imaging object. The SNR is similar to the CNR, but takes into consideration the shape of the object as

well as the size of it. This way, the test object does not have to be homogeneous. The SNR includes the sum of the signals at each pixel [26, pp. 91-92].

Contrary to artefacts, which will be seen on an image at the same position and in the same intensity and appearance for a repetition of measurements, noise is a probabilistic phenomenon. It describes the degradation of image quality due to physical events like the creation of the X-ray beam and interactions of the photons with matter like scatter [20], which are random effects. Due to this fact, noise is seen as random fluctuations of the signal at the detector. The SNR is proportional to the number of photons used. More photons hit the detector when higher energy settings are used. This is due to less attenuation and as a consequence less dose for the patient. The noise in an image decreases with a larger number of photons at the detector and the SNR increases [28].

Not only is the quantification of the noise of significance. The texture of the noise impacts image quality too. In order to characterize the amplitude of the probabilistic noise the variance is often used. In order to quantify the texture of the noise, which is a way to describe the look of the noise in an image, the noise power spectrum (NPS) is used. The NPS is a function of the frequency in both the x- and the y-dimension and its integral over all frequencies is equal to the variance. This dependency on the position is a consequence of noise in one detector element bleeding to the surrounding elements. On the other hand, constant noise for all detector elements is called white noise. A graph of the NPS can be drawn depending on the spatial frequency in cycle/mm and depicts a decreasing function [26, pp. 86-87].

There are multiple sources of noise in a medical image. For screen-film mammography, grain noise can appear in the image as small darker spots in exposed brighter areas not visible to the human eye without any aid. It results from the random arrangement of the silver particles due to the manufacturing process of the film and later the processing of the image. It should be noted that magnification glasses are commonly used to detect small particles in clinics and reveal the presence of grain noise. Electronic noise on the other hand is observed in both analogue and digital mammography. It describes added current in the form of additional electrons occurring from thermal heat or electronic components in the X-ray imaging geometry and is observed as an offset of the detected signal. This type of noise is especially problematic when the signal and hence the noise is amplified and when the original signal is low. Anyhow, cooling and shielding can reduce this type of noise. Anatomical noise results from the anatomy of the patient with structures overlapping important tissue. This problem is solved by 3D imaging techniques. Structured noise can only be seen for digital detectors and represents itself as a pattern of shifted objects. This offset in signal and position can be fixed by algorithms altering the final image based on another correction image taken beforehand. A spatial shift in structures in the image results from the readout mechanism of digital detectors. The detector element arrays may be out of sync. Even within the individual pixels, offsets may be observed and corrected by algorithms and the calibration of the detector. Finally, quantum noise is especially prominent in mammography with its low dose. Quantum noise is a result of the statistical distribution of quanta, which is a term for countable

particles. X-ray photons are used in mammography and fall under the term of quanta. The photons hit the detector randomly, causing increased quantum noise when a lower number of photons is used [26, pp. 77-80].

Another indicator of image quality is the level of detail that can be imaged. The limiting spatial resolution gives the smallest feature that can be seen on an image. When this detectability is assessed for a continuous spectrum of the object size with a high dose and subsequently less noise, the modular transfer function (MTF) can be used. It gives the loss in contrast depending on the spatial frequency of the object as well as the image quality produced by the imaging unit as a result. Spatial frequencies correspond to the size of an object. For low spatial frequencies the object is big and the grey values do not change often. High spatial frequencies on the other hand stand for small objects with fast and drastic changes in the image. The MTF ranges from 0 to 1 and is the highest for small spatial frequencies and decreases with increasing frequencies as smaller objects exhibit worse contrast. The imaging unit is not able to image smaller objects and the limiting spatial resolution marks the smallest feature size and the biggest spatial frequency the imaging unit can depict [26, pp. 70-72] [41]. The MTF of an imaging geometry is assessed with the Fourier transfer of the line spread function (LSF). The LSF gives the grey value amplitude of a line as the input signal depending on the position in the y-direction. If the spatial resolution of the system is good, the function of the LSF is thin and the line is depicted with a small range of pixels [26, pp. 63-64]. The Fourier transfer is used to transition from the frequency domain to the spatial domain. The line input of the LSF is equal to sinusoidal functions on the whole the frequency spectrum in the frequency domain. The MTF gives the reduction of these sinusoidal signals depending on their frequency [26, p. 72].

The MTF is measured imaging a slanted edge, which is produced using a rectangular steel plate positioned slightly off. In Austria, measurements of the MTF utilizing a slanted edge and the CNR assessed with a squared aluminium plate as the feature are included in the instructions for mandatory quality assurance tests on mammography units and evaluated by AGES, the Austrian association responsible for testing mammography units in Austria and ensuring quality for the government funded mammography screening program [61]. It should be noted that using mathematical functions, which are measured from test images, is an objective way to find image quality and makes these indicators more comparable and reliable. Still, it needs to be added that some measurements can be difficult to conduct and might influence the results. A good example is the measurement of the MTF, which also includes assumptions on the imaging system and its characteristics [59].

1.2.2 Current contrast quality assessment using phantoms

Because of the high number of mammography examinations, it is essential to control image quality and to test for object detectability. Control organizations like EUREF and AAPM created protocols using phantoms as test objects for FFDM. These phantoms are used to test for the detectability of lesions, which are assessed by human readers

or computerized evaluations [16]. Phantoms for medical imaging are produced in order to simulate a response from the imaging unit that is similar to the average patient in terms of attenuation. Requirements for these phantoms include being transportable and economical, while being consistent. Their results need to be comparable, representative and independent of the imaging unit and its manufacturer [62]. Furthermore, phantoms should be valid, reproducible, objective, sensible for dose and suited for the imaging modality. As human readers are highly uncertain, it is better to use model observers [42].

The standard for quality assessment in mammography written down in the current edition of the European Guidelines for Quality Assurance in Mammography Screening of the European Union is applied in most countries and recommends the use of the CDMAM phantom [63]. The CDMAM phantom consists of a uniform background and gold discs of varying size and thickness (see Figure 1.9). The 410 gold discs' diameter increases exponentially from 0.06 to 2 mm and the thickness ranges from 0.002 to 0.03 mm. Due to the high number of test objects, a satisfying accuracy can be achieved compared to other phantoms. The reader finds the smallest readable thickness for each size, which is called threshold thickness. The smallest detectable contrast is then plotted depending on the diameter of the discs describing the contrast-detail curve. This plot shows the relationship between threshold thickness and the diameter. For this phantom it should be noted that the results highly depend on the reader. High inter- and intra-observer variabilities are noticed. Secondly, the human reader might remember the positions of the discs and anticipate the signal. There are two discs per thickness and diameter, arranged in a way that there is one disc in the middle of the square and the second one in one of the four corners. This random positioning aims at minimizing the chance of the reader to assessment by memory and to decrease threshold thickness. However, it is advised to use computer readers instead of human observers to eliminate this problem [22, pp. 469-470] [64].

In the USA, the ACR phantom is widely used. It provides the reader with a homogeneous background made out of wax with 3 types of lesions [16]: monofilament nylon fibres, simulated microcalcifications made of spherical glass and spherical mass particles with 10% adipose tissue and 90% glandular tissue. The wax is embedded in a PMMA block. It is used for tests of FFDM units [66]. This phantom is produced at a low price and popular due to its simple structure and the resulting fast measurements. But it should also be noted that the limited number of test features in the phantom is a disadvantage and has shown to perform poorly in tests [64].

Besides the two mentioned phantoms, there are other phantoms. Their differences lie in their homogeneous or heterogeneous backgrounds, the inclusion of microcalcifications or mass features for contrast-detail tests and the question, whether the phantom can be stacked. To name some examples the Mammographic Accreditation Phantom by the company Computerized Imaging Reference Systems, the MTM100 Breast Phantom by Meditron and the TOR MAM Mammography Phantom by Leeds Test Objects can be bought for FFDM. They all have a homogeneous background, with the TOR MAM phantom also providing a heterogeneous background. They all provide structures for

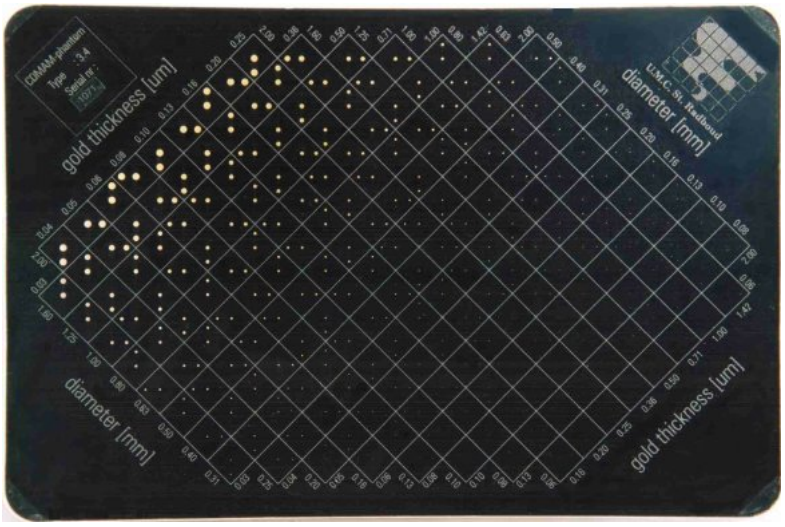

Figure 1.9: An image of the CDMAM phantom consisting of a uniform background and gold discs of varying size and thickness in order to assess image quality in terms of detail detectability. Source: [65]

contrast-detail tests, but the TOR MAM also includes fibres and microcalcifications besides masses in the homogeneous half of the phantom and microcalcifications in the heterogeneous part. The QUART mam/digi EPQC by the company QUART provides the reader with no masses on a homogeneous background, but with contrast numbers on multiple PMMA plates.

For DBT the Tomophan phantom by The Phantom Laboratory, the Digital Breast Tomosynthesis QC Phantom by Computerized Imaging Reference Systems, the TOMO-MAM 3D by Orion France, the Modular DBT Phantom by Sun Nuclear, the VOXMAM phantom by Leeds Test Objects and the BR3D Breast Imaging Phantom again by Computerized Imaging Reference Systems are on the market. The last two phantoms have a heterogeneous background, while the others have a homogeneous one. The Modular DBT Phantom and the Digital Breast Tomosynthesis QC Phantom however consist of plates showing 50% fat and 50% ductal tissue and the later can be enhanced with a heterogeneous plate. This makes them stackable like the BR3D phantom. All phantoms for DBT have test objects for contrast-detail tests except for the VOXMAM phantom, which only has 4 groups of microcalcifiactions at random and unknown positions. The BR3D phantom has additional microcalcifications and masses [42].

When looking at the rules applied in Austria by AGES, the CDMAM phantom can be found in the instructions for the yearly quality assessment tests. This follows the EUREF-Ö rules that are in place in Austria. The phantom is used in measurements regarding contrast resolution in-between PMMA blocks. The threshold thickness is evaluated by AGES after the images are sent in. For tomography systems an additional measurement has to be done. The CDMAM is used with 3 blocks of PMMA. With 3

different positions of the phantom in-between the blocks, measurements of 3 different geometries are taken. Then the plane in which the phantom's gold discs can be seen and distinguished for a set diameter and thickness are found. This tests the results of the reconstruction for the horizontal planes and has to be done if DBT images are taken with patients. However, it is stated in the guidelines that test regarding DBT are in a piloting stage and there are no specific phantoms for this modality mentioned [67] [61].

1.2.3 The novel L2 phantom

For the CDMAM and ACR phantom, which are the most used phantoms in quality management regulations and that are described in chapter Current contrast quality assessment using phantoms, it has to be noted that their homogeneous backgrounds are not suitable for quality control since they neglect the anatomy of the human breast [16]. When using a heterogeneous background that is static, the results of computerized readout done with artificial intelligence can be altered as the program might learn to detect the lesions based in the background. A changeable, non-static, heterogeneous background mimicking the human breast and the different tissue types involved would be ideal and hence minimize the risk of the computerized reader to base their detection based on the background of the phantom [42].

Considering these points, the novel L2 phantom was created at the Medical University of Vienna in cooperation with KU Leuven (Leuven, Belgium). This L2 phantom is the second iteration of the L1 phantom proposed in [16]. The L2 phantom (see Figure 1.10) consists of a chasing made of PMMA in a semicircle form with a diameter of 24 cm. It is 53.5 mm high and filled with PMMA spheres of six diameters ranging from 1.6 mm to 16 mm embedded in paraffin oil. Shaking the phantom results in a change of background as the spheres move around in the liquid. This way a non-static 3D structure is achieved, which makes the phantom suitable to test for masking happening when there is overlapping tissue and with observer models [42] [18].

The phantom is not stackable. At mid-height a 3D-printed plate is inserted into the phantom. On the plate features for contrast-detail tests are embedded. There are ten non-spiculated mass models derived from a tumour database with diameters ranging from 1.4 to 6.1 mm. Besides, there are five groups of microcalcifications with six particles each. Their sizes go from 125 to 224 µm (see Table 1.1). They are arranged with one particle in the middle and the other five particles in the corners of a pentagon around the centre particle (see Figure 1.11) [42] [18].

The dose sensitivity of the microcalcification and the mass models included in the phantom was assessed in a previous step, which is a crucial point to decide on the usability of the phantom in clinical quality tests [18]. Also the detectability of the two target materials was tested and compared for the L1 phantom with FFDM and DBT and showed high detectability for both modalities with DBT giving better results [16]. This thesis shall now take on the next tasks of validating the microcalcification as one of the two test features found in the L2 phantom.

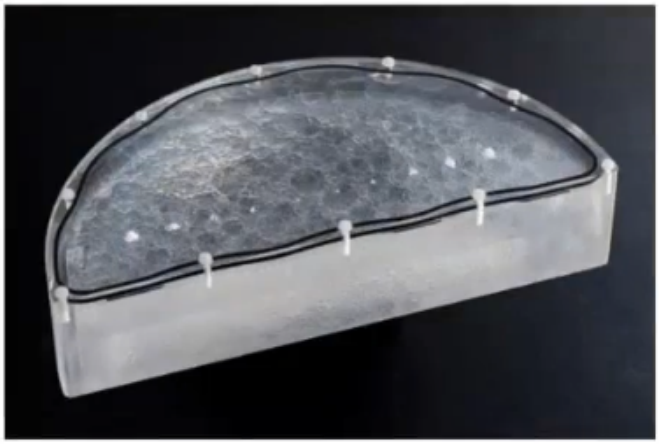

Figure 1.10: An image of the novel L2 phantom consisting of the visible mass models and microcalcifiations, which are not visible from this view angle, embedded in PMMA spheres in paraffin oil. The case is made of PMMA. Source: [42]

Table 1.1: The five size groups of the microcalcifications included in the L2 phantom with their minimum and maximum diameter in µm.

Size group	Minimum diameter [µm]	Maximum diameter [µm]
0	200	224
1	180	200
2	160	180
3	140	160
4	125	140

1.3 Virtual clinical trials

The standard method to test imaging methods and their potential advantage is to conduct clinical trials. Clinical trials are experiments conducted with human subjects. Yet, they are expensive in terms of money and time and sometimes challenging due to ethical limits. In order to test new concepts and ideas easily and fast, virtual clinical trials (VCTs) have gained attraction. Virtual clinical trials are in-silico replacements or copies of clinical examinations. This includes the use of mathematical and computational models to simulate medical examinations. For the investigation and the comparison of imaging techniques, a high number of patients and imaging facilities that are needed for statistical significance as well as personal to take the images and to coordinate these trials. Moreover, the increased patient dose should be considered. The risk of unnecessary and high patient dose is eliminated with VCTs where the entire imaging process with the imaging object, imaging system and the radiological interpretation is virtually modelled. Often model observers mimicking human observers are applied [68] [69] [70]. One additional advantage

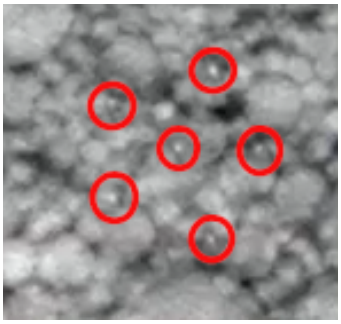

Figure 1.11: The six microcalcifications with one in the middle and five in the corners of a pentagon (see red circles) of the L2 phantom fixated on the plate in the phantom with a heterogeneous background. Source: Adapted from [42]

of VCTs is their flexibility in terms of input parameters, which can be adjusted to the improving depth and accuracy of the imaging systems resulting from rapid advancements in research. Tests can be done comfortably and fast with a high number of different settings. Examples include the used exposure or the imaging units. The results of these inputs can later be compared and interpreted [51]. The use of virtual clinical trials also challenge the use of physical phantoms. These phantoms do not represent clinical settings and are mostly rather simple in their setup [70].

Connected to the idea of a simulation of the whole imaging process, simulation frameworks for multiple test objects are created and used. They can simulate the breast's anatomy and lesions as well as the application of image processing. Furthermore they can simulate the display of the images, their evaluation and the radiological acquisition [49].

1.3.1 The simulation tool

Keeping the advantages of VCTs in mind, a simulation framework for the insertion of lesions into FFDM and DBT breast images was created by KU Leuven (Leuven, Belgium) and verified for the imaging unit Siemens Inspiration in the 2D and 3D mode. The tool first creates an ideal template of a lesion based on the background, the lesion size and form, the attenuation coefficient of the material, the imaging system, the position of the particle and the energy spectrum utilizing ray tracing and spectrum simulation. Then the template is modified with the introduction of scatter and a resolution matching the imaging system. This modified template is inserted into the raw projections, which are reconstructed to a 3D image (see Figure 1.12) [49]. Ray tracing tools compute the path of an X-ray photon traveling through a volume. This results in a mathematical description of the path of the photon along the projection from the source to the detector and of the intensity of the photon along this path. The output of a ray tracing tool depends on the spectrum simulation of the X-ray imaging system. The X-ray spectrum yields the distribution of the attenuation measured on the detector. The X-ray spectrum can be found with Beer-Lambert's law, Equation 1.3, which depends on the length of the

volume and the energy- and material-dependent attenuation coefficient, and gives the attenuation values of the photons. Some characteristics of the imaging units that are used are the kVp and dose, the filter, the source to image distance, the detector dimensions and the information about the compression paddle [51] [71] [72]. Ray tracing algorithms are seen as advantageous due to their computational efficiency when calculating the projections of the lesions based on Beer-Lambert's law. However, they do not include scatter simulations. They are often added in the following steps [69].

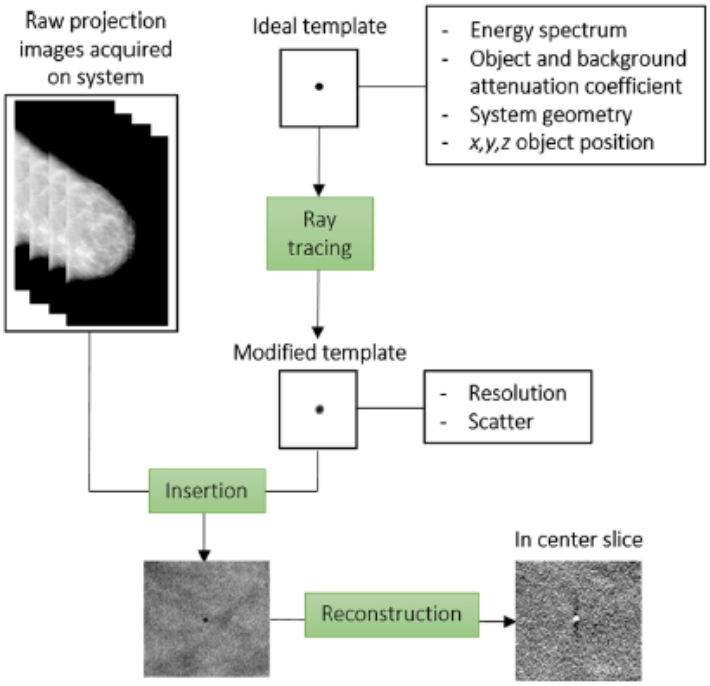

Figure 1.12: The logic of the used simulation framework for VCTs. The ideal template of a lesion is created and modified with ray tracing and spectrum simulation and then inserted into the raw projection images, which can be reconstructed as the last step. Source: [49]

The user is given a graphical user interface to provide the input values for the simulation (see Figure 1.13). The simulation process starts with the menu "Preparation". The input values include the tomography system, the structure to be simulated and its size and the attenuation coefficient. The attenuation coefficient can be a measured value that is typed in or simulated with more information about the tissue, background and material (see Figure 1.14). This includes choosing a simulated and a background material from a drop-down menu or a mixture of two materials. The attenuation coefficients for the materials depending on the kV settings are included in the simulation tool's data files. Lastly, for the breast type a real breast is distinguished from PMMA and the thickness is specified in cm. The tomosynthesis geometry is chosen while the user is provided with

an overview of the important geometry and detector preferences. After this information is given, the ray tracing process can be started by selecting the central 13th projection projection of the raw images. This creates a folder with a txt-file containing the important information about the simulation and one raw-file per projection as a template for the second process, the insertion.

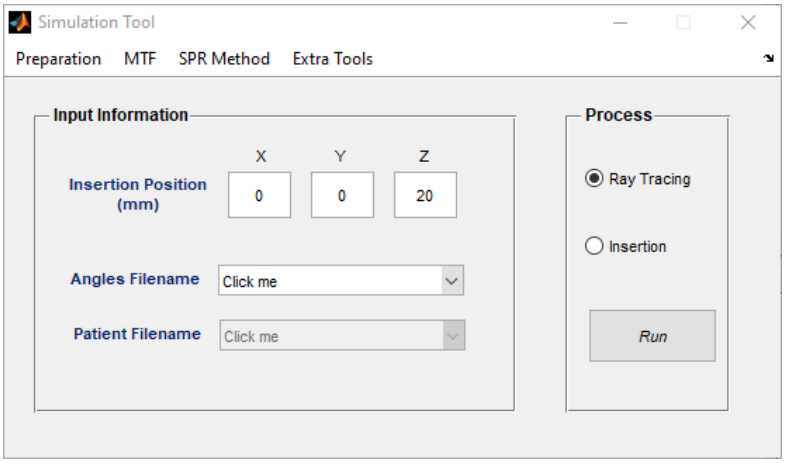

Figure 1.13: The graphical user interface of the simulation tool in MATLAB described in [49]. The user can specify the imaging system and the particle to simulate with the menu "Preparation", type in the position of the particle and first do ray tracing and then the insertion after the MTF and the SPR method for the imaging system are defined.

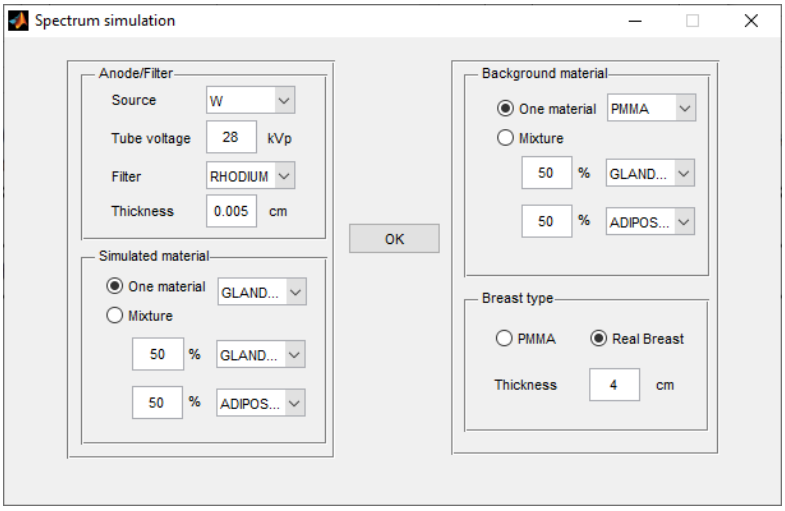

Figure 1.14: The graphical user interface of the MATLAB simulation tool introduced in [49], where the spectral simulation for the attenuation coefficient can be defined. The user is asked to characterize the simulated and the background material, the characteristics of the X-ray tube and the breast.

For the insertion, the MTF and its coefficients are measured for each imaging system and selected as an Excel sheet as an input. The MTF alters the resolution of the particle, as the results of the ideal simulation exhibit a resolution that is too high. The information txt-file is then multiplied by the MTF and new MTF corrected templates are created for each projection. Lastly, the SPR method is chosen depending on the imaging system, the in- or exclusion of a grid is decided. For DBT there is no anti-scatter grid applied. If the image is done in 2D, the option "grid in" has to be selected for the SPR. With these inputs, a value for the SPR is automatically found depending on the thickness of the breast and the imaging system. Then the insertion can take place, choosing the same central projection as the patient filename and applying the information txt-file. This way a final folder is created with all projection of the finished simulation. These projection can next be resonstructed to the 3D image.

CHAPTER 2

Materials and Methods

2.1 Used materials

The simulation of the microcalcification was done in MATLAB 2013b [73] using the 7th version of a simulation tool [49], which was programmed for this version of MATLAB, and a Microsoft Excel sheet [74] to calculate the input for the simulation tool. Both were provided by KU Leuven (Leuven, Belgium). ImageJ 1.53e [75] was used to measure the MPV in ROIs saved via the ROI manager of ImageJ as well as the positions of the particles. Lastly, Microsoft Excel was used again in order to save the results and process them calculating the mean, standard deviation and contrast.

The images used for the measurement were provided by the Center for Medical Physics and Biomedical Engineering of the Medical University of Vienna. They were taken with the Siemens Healthineers Mammomat Inspiration (Siemens Healthcare GmbH, Erlangen, Germany) of the General Hospital of Vienna and consist of images of a 4 cm PMMA block with microcalcifications spread across and another images with only the block. The images were taken with the Mammomat Inspiration with an exposure of 19.8 mAs (DICOM tag 0018,1153) and 28 kVp (DICOM tag 0018,0060).

2.2 Execution of the virtual clinical trial

In order to test the contrast of the microcalcifications in the phantom, two images of 4 cm PMMA were provided. One DBT image shows the PMMA block and was used for the simulation. The second one included the 5 classes of microcalcifications spread on the PMMA. Their size class was marked with screws being responsible for the circles on the left side of the PMMA (see Figure 2.1).

The diameter used for the simulations of each size group is the mean of the range per

group and was calculated following

$$\mu = \frac{\sum_{i=1}^{N} x_{\mathrm{i}}}{N}, \tag{2.1}$$

with $x_{\max} + x_{\min}$ being $\sum_{i=1}^{N} x_{\mathrm{i}}$ in the case of $x_{\max}$ being the maximum diameter for the size class and $x_{\min}$ being the minimum size resulting in $N = 2$. This leads to Table 2.1, which gives the mean diameter for each size group based on Table 1.1 and was then used as the diameters of the simulated spheres.

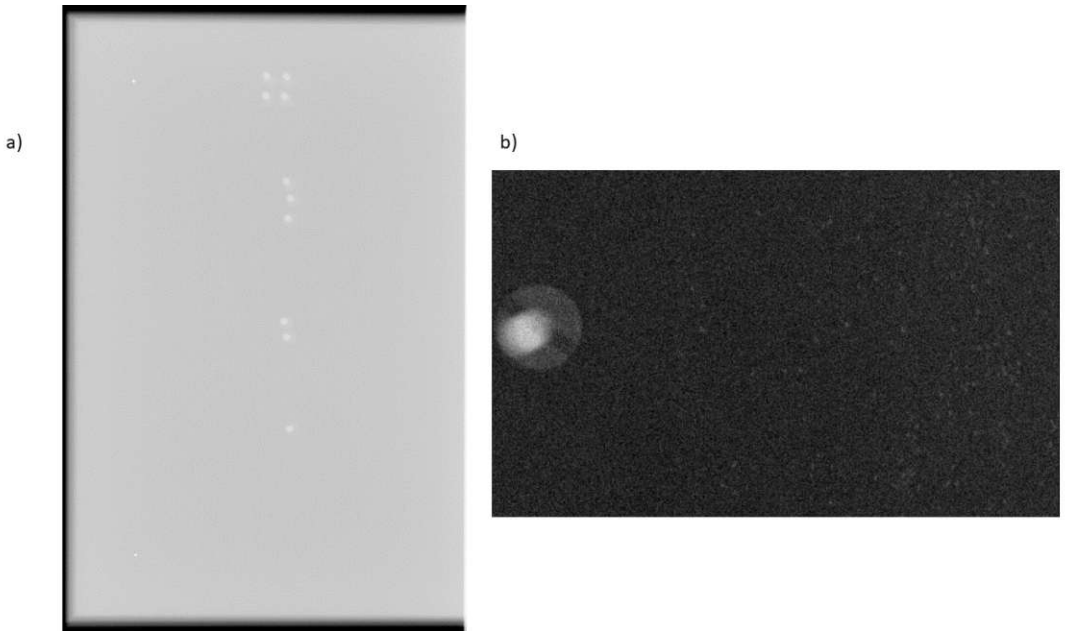

Figure 2.1: The 13th projection of 4 cm PMMA with the five size classes of microcalcifications spread on the surface. Figure a) shows the whole PMMA block with the screws giving the size classes and the microcalcifications to the right. Figure b) offers an amplified look at the size class 1. The image was also adjusted with the window/level functionality of ImageJ. The particles can be seen in white to the right of the round screw.

For the measurement of the positions and the MPVs the 13th central projection was used (see Appendix A: Positions of the particle measurements for the coordinates of the particles). The projection with the number 0 of the DBT image was omitted. The Mammomat Inspiration produces 25 projection and adds another projection with the number 0 mimicking the central projection at 0°. The simulation tool however expects only 25 projections. The positions and the MPVs of 20 randomly chosen particles per size class were measured with ROIs of 3 pixels × 3 pixels. Using an Excel sheet provided by KU Leuven (Leuven, Belgium) the positions of the microcalcifications measured with ImageJ were converted to coordinates in MATLAB images, which were used as the inputs for the simulation tool. This conversion file asks for the detector primary angle,

Table 2.1: The five size groups of the microcalcifications included in the L2 phantom with their mean diameter in µm.

Size group	Mean diameter [µm]
0	212
1	190
2	170
3	150
4	132.5

which is -1.63° for the 13th projection, and the z position of the particle, which was recommeneded by KU Leuven to be 20 mm. The same was done for 4 background ROIs per particle ROI, which results in 80 background ROIs per size group (see Appendix B: Positions of the background measurements for the positions of the ROIs for the background measurements). The size of the background particles

The MATLAB simulation tool asks for distinct inputs in order to simulate the wanted particle following measured data about different imaging units in the graphical user interface. Firstly, the tomosynthesis system is chosen to be "Siemens Inspiration" with the drop-down menu option "Preparation" and then "Tomo System". In the same menu the 3D object is chosen to be a sphere and the diameter is entered per size group in mm following Table 2.1. Lastly, the attenuation coefficient is modelled with the option "Spectrum simulation". There the simulated material is chosen to be "Ca Carbonate", the background material is set to one material PMMA and the breast type is defined as PMMA with 4 cm thickness. Next, the position of the particle is defined following Appendix C: X- and y-coordinates for the simulation, where the converted x- and y-coordinates of the feature ROIs can be found. The "Angles Filename" is the 13th projection of the image of the bare PMMA block. The process "Ray Tracing" is run and the templates are saved.

In the next step the menu "MTF" and then "Load coeff. file" is selected. This way an Excel file provided by KU Leuven is supplied to the program. With the menu option "Multiply by MTF" the txt-file created from the ray tracing process is selected and modified. This creates a new folder containing the 25 templates of the simulation with a modified resolution. Then, the "SPR Method" is chosen to be "Elena", "Siemens Inspiration" and "Grid OUT". As the last step, "Insertion" is selected as the process and the "Patient Filename" is again the 13th projection of the image of the PMMA block. Once more, the simulation tool asks for the txt-file, which is selected. The final 25 projections incorporating the simulation of the microcalcification particles are saved in a new folder called "Simulated". The described simulation process is repeated for all 100 particles, taking the 13th projection of the preceded simulation output as the new "Angles Filename" and "Patient Filename". This way the final simulation contains all 100 particles.

The contrast was calculated following Equation 1.6 for the 20 signals and their back-

grounds. The background is the average (see Equation 2.1) of the MPVs of four 3×3 pixel ROIs two pixels away from the ROI containing the signal in the x- and y-direction respectively (see Figure 2.2). Lastly, the standard deviation is calculated with

$$\sigma = \sqrt{\frac{1}{N}\sum_{i=1}^{N}(x_\mathrm{i} - \mu)^2}, \tag{2.2}$$

containing the contrast values as x_i and the mean of them as μ calculated with Equation 2.1. For the comaprision of the simualtion to the original image, the difference of the 20 contrast measurements was found and then averaged per size group with Equation 2.1.

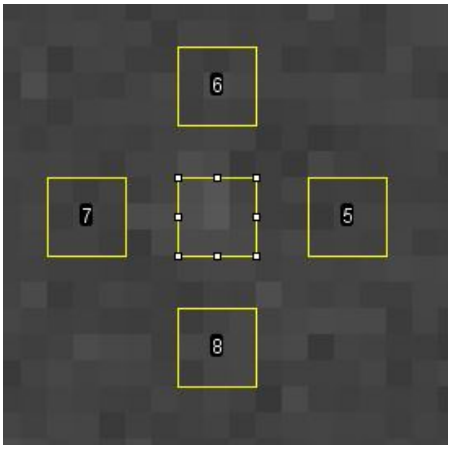

Figure 2.2: An image of the 4 background ROIs with the numbers 5, 6, 7 and 8 surrounding the feature measured with the unnumbered ROI in the middle. The 13th projection of the original DBT measurement with the real microcalcifications was modified with the window/level functionality in ImageJ.

CHAPTER 3

Results

20 randomly chosen ROIs of the size of 3 pixels × 3 pixels were found for all five size classes in the 13th projection of the image with the microcalcifications on 4 cm PMMA. The x- and y-coordinates of the ROIs for the particles of each size class can be found in Appendix A: Positions of the particle measurements. The x- and y-positions of the 4 background ROIs per particle can be found in Appendix B: Positions of the background measurements. The mean of these 4 MPVs (which are featured in Appendix D: Mean pixel values of the background results in a measure of the background, which can be found in Table 3.1, Table 3.3, Table 3.5, Table 3.7 and Table 3.9 together with the MPVs of the particles for both the original image with the real microcalcifications and the image of the simulations in an empty PMMA block. For the insertion the calculated mean particle diameter in Table 2.1 and the transformed input positions in Appendix C: X- and y-coordinates for the simulation utilizing the Excel sheet by KU Leuven were used. In Figure 3.1 a selection of the 20 simulations for the biggest size group 0 can be found. The particles appear as white on the background. The image was adjusted with the window/level functionality in ImageJ in order to improve the visibility of the particles.

Utilizing the MPVs of the background and the microcalcifications, the local contrast is found for the original and the simulated image by using Equation 1.6 (see Table 3.2, Table 3.4, Table 3.6, Table 3.8 and Table 3.10). The mean of the MPVs for the four background ROIs is used. The variation is equal to the standard deviation (see Equation 2.2). The average of the absolute values of the difference in contrast is calculated per size group in order to compare (see Table 3.11).

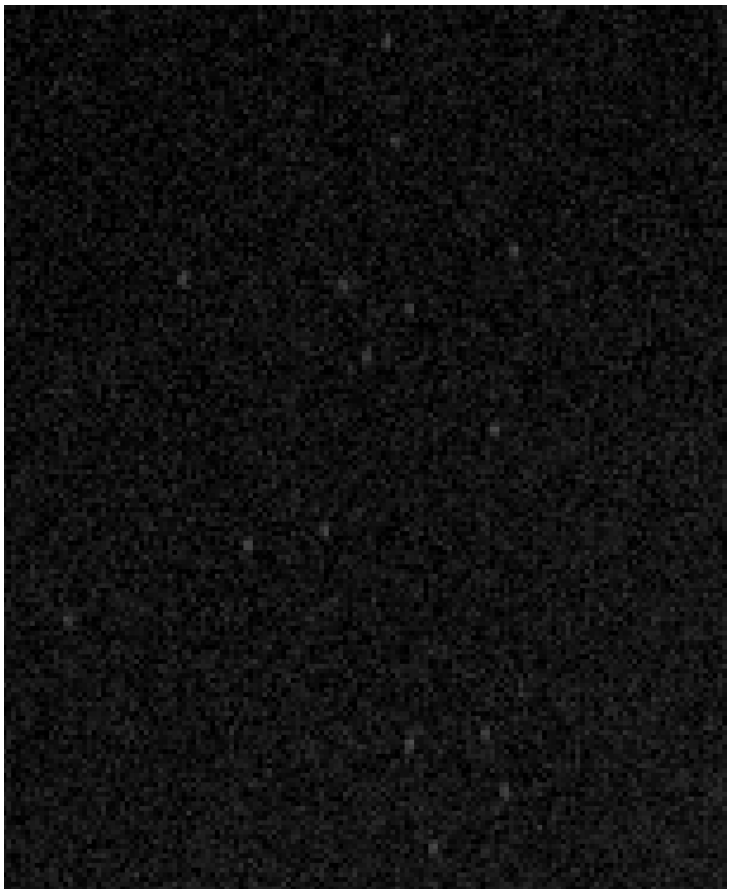

Figure 3.1: A selection of the simulations of the size group 0 in the 13th projection as white particles. ImageJ's window/level functionality is used in order to improve the visibility of the microcalcifications.

Table 3.1: The MPV measurements of the background and the particle of the 20 microcalcifications of the size group 0 in the 13th projection.

	Original		Simulation	
Particle	MPV particle	MPV background	MPV particle	MPV background
1	525.556	551.194	523.556	550.195
2	522.333	552.833	524.667	547.139
3	529.333	554.445	530.222	548
4	521.222	552.139	523.111	554.611
5	522.333	552.417	527	551.695
6	519.778	543.111	518	544.722
7	528.333	553.695	523.111	552.389
8	508.222	544.750	512.778	545.111
9	524.333	552	524.111	554.500
10	514.222	538.278	516.444	540.361
11	517.222	545.334	517.444	544.083
12	518.667	548.806	521.333	548.583
13	505.444	539.167	509.222	533.778
14	518.778	553.111	522.444	550.528
15	522.889	551.556	525.111	546.472
16	522.778	553.361	521.889	552.084
17	522	555.972	524.667	554.278
18	516	548.722	519.444	544.306
19	513.333	548.528	516.778	548.694
20	521.889	547.528	522.889	540.945

Table 3.2: The local contrast of the original image and the simulation of the 20 microcalcifications of the size group 0 in the 13th projection and the absolute value of the difference.

Particle	Contrast original	Contrast simulation	Absolute difference
1	-0.0465	-0.0484	0.0019
2	-0.0552	-0.0411	0.0141
3	-0.0453	-0.0324	0.0128
4	-0.0560	-0.0568	0.0008
5	-0.0545	-0.0448	0.0097
6	-0.0430	-0.0491	0.0061
7	-0.0458	-0.0530	0.0072
8	-0.0671	-0.0593	0.0077
9	-0.0501	-0.0548	0.0047
10	-0.0447	-0.0443	0.0004
11	-0.0515	-0.0490	0.0026
12	-0.0549	-0.0497	0.0052
13	-0.0625	-0.0460	0.0165
14	-0.0621	-0.0510	0.0111
15	-0.0520	-0.0391	0.0129
16	-0.0553	-0.0547	0.0006
17	-0.0611	-0.0534	0.0077
18	-0.0596	-0.0457	0.0140
19	-0.0642	-0.0582	0.0060
20	-0.0468	-0.0334	0.0134

Table 3.3: The MPV measurements of the background and the particle of the 20 microcalcifications of the size group 1 in the 13th projection.

	Original		Simulation	
Particle	MPV particle	MPV background	MPV particle	MPV background
1	536.556	550.750	536	550.083
2	529.222	549.444	533	554.333
3	531.222	553.333	532.889	555.083
4	532	550	534	554.639
5	533.889	551.195	535.333	555.556
6	533.333	552.917	532.444	555.306
7	531.889	553.028	529.889	556.084
8	536.333	550.722	536.111	551.445
9	530	554.417	528.556	556.028
10	537.778	556.611	538.778	557.889
11	535.889	555.778	536.333	556.472
12	532.889	556.722	531	551.222
13	531.333	555.417	530.889	553.611
14	536	553.305	536.111	555.722
15	532.778	558.056	533.778	558.000
16	530.889	550.750	535.333	551.084
17	530.444	552.472	534.778	557.500
18	533.667	552.667	532.667	552.556
19	532.222	546.639	531.667	555.806
20	535.222	548.694	534.222	553.722

Table 3.4: The local contrast of the original image and the simulation of the 20 microcalcifications of the size group 1 in the 13th projection and the absolute value of the difference.

Particle	Contrast original	Contrast simulation	Absolute difference
1	-0.0258	-0.0256	0.0002
2	-0.0368	-0.0377	0.0009
3	-0.0400	-0.0400	0.0000
4	-0.0327	-0.0372	0.0045
5	-0.0314	-0.0364	0.0050
6	-0.0354	-0.0412	0.0058
7	-0.0382	-0.0471	0.0089
8	-0.0261	-0.0278	0.0017
9	-0.0440	-0.0494	0.0054
10	-0.0338	-0.0343	0.0004
11	-0.0358	-0.0362	0.0004
12	-0.0428	-0.0367	0.0061
13	-0.0434	-0.0410	0.0023
14	-0.0313	-0.0353	0.0040
15	-0.0453	-0.0434	0.0019
16	-0.0361	-0.0286	0.0075
17	-0.0399	-0.0408	0.0009
18	-0.0344	-0.0360	0.0016
19	-0.0264	-0.0434	0.0171
20	-0.0246	-0.0352	0.0107

Table 3.5: The MPV measurements of the background and the particle of the 20 microcalcifications of the size group 2 in the 13th projection.

	Original		Simulation	
Particle	MPV particle	MPV background	MPV particle	MPV background
1	539.778	555.667	543	558.750
2	537.222	554.861	537	553.139
3	538.778	553.361	541.556	553.445
4	538	553.778	541.889	562.222
5	538.556	555.583	538.111	555.056
6	539.556	552.055	536.222	557.500
7	536.889	553.722	538.667	548.639
8	534	554.750	539	553.778
9	538	554.917	540.333	559.416
10	536.333	552.694	536.667	550.361
11	542.556	555.139	542.556	553.056
12	535.667	548.500	536.333	552.306
13	541.556	550.556	545.556	557
14	541.667	549.972	540.667	554.417
15	543.889	553.556	544.889	554.917
16	539.444	553.306	541.333	554.333
17	544.333	551.306	546.556	557.806
18	539.111	553.639	541.667	555.945
19	543.667	550.111	545.111	556.444
20	536	555.445	537.333	553.250

Table 3.6: The local contrast of the original image and the simulation of the 20 microcalcifications of the size group 2 in the 13th projection and the absolute value of the difference.

Particle	Contrast original	Contrast simulation	Absolute difference
1	-0.0286	-0.0284	0.0002
2	-0.0318	-0.0288	0.0030
3	-0.0264	-0.0215	0.0049
4	-0.0285	-0.0362	0.0077
5	-0.0306	-0.0305	0.0001
6	-0.0226	-0.0382	0.0155
7	-0.0304	-0.0182	0.0122
8	-0.0374	-0.0267	0.0107
9	-0.0305	-0.0341	0.0036
10	-0.0296	-0.0249	0.0047
11	-0.0227	-0.0190	0.0037
12	-0.0234	-0.0289	0.0055
13	-0.0163	-0.0205	0.0042
14	-0.0151	-0.0248	0.0097
15	-0.0175	-0.0181	0.0006
16	-0.0251	-0.0235	0.0016
17	-0.0126	-0.0202	0.0075
18	-0.0262	-0.0257	0.0006
19	-0.0117	-0.0204	0.0087
20	-0.0350	-0.0288	0.0062

Table 3.7: The MPV measurements of the background and the particle of the 20 microcalcifications of the size group 3 in the 13th projection.

	Original		Simulation	
Particle	MPV particle	MPV background	MPV particle	MPV background
1	547.444	551.472	549.111	551.111
2	543.111	551.972	548.444	551.806
3	545.889	549.056	548.778	554.028
4	547.556	553.361	547.556	552.584
5	544.889	554.528	549.556	552.306
6	539	554.083	539.667	556.584
7	545.778	555.917	548.333	553.195
8	549.333	557.361	549.111	558.083
9	545.667	553.111	547.889	554.667
10	548.889	555.250	549.222	553.389
11	553	557.361	553.111	558.444
12	550	558.722	554	555.556
13	543.111	553.972	543.889	552.583
14	547.444	554.028	547.556	557.667
15	546.556	559.972	548.556	557.056
16	555.333	556.722	554	558.917
17	550.111	562	553.667	559.306
18	546.556	554.111	549.444	554.028
19	540.222	552.167	543.444	553.500
20	550.556	558.195	550.222	558.917

Table 3.8: The local contrast of the original image and the simulation of the 20 microcalcifications of the size group 3 in the 13th projection and the absolute value of the difference.

Particle	Contrast original	Contrast simulation	Absolute difference
1	-0.0073	-0.0036	0.0037
2	-0.0161	-0.0061	0.0100
3	-0.0058	-0.0095	0.0037
4	-0.0105	-0.0091	0.0014
5	-0.0174	-0.0050	0.0124
6	-0.0272	-0.0304	0.0032
7	-0.0182	-0.0088	0.0094
8	-0.0144	-0.0161	0.0017
9	-0.0135	-0.0122	0.0012
10	-0.0115	-0.0075	0.0039
11	-0.0078	-0.0096	0.0017
12	-0.0156	-0.0028	0.0128
13	-0.0196	-0.0157	0.0039
14	-0.0119	-0.0181	0.0062
15	-0.0240	-0.0153	0.0087
16	-0.0025	-0.0088	0.0063
17	-0.0212	-0.0101	0.0111
18	-0.0136	-0.0083	0.0054
19	-0.0216	-0.0182	0.0035
20	-0.0137	-0.0156	0.0019

Table 3.9: The MPV measurements of the background and the particle of the 20 microcalcifications of the size group 4 in the 13th projection.

	Original		Simulation	
Particle	MPV particle	MPV background	MPV particle	MPV background
1	543.667	547.833	548.333	551.056
2	534.111	547.611	544.222	546.556
3	540.778	549.278	544.333	548.417
4	549.111	551.083	552.667	549.889
5	546.556	547.111	547.222	548.083
6	542.556	546.334	543	547.333
7	538.667	538.889	542.111	548.250
8	541.222	547.139	543.667	550.945
9	546.222	543.139	549	545.611
10	543.111	550	546.889	550.361
11	543.556	547.278	543.222	549.111
12	538.111	545.139	538.222	547.417
13	537.333	541.722	538.222	548.139
14	539.222	545.917	541.889	551.556
15	538.889	547.472	540.111	545.195
16	540.444	549.973	542.111	551.611
17	546.333	546.750	545.556	550.973
18	543	549.500	545.556	544.722
19	545.667	544.389	547.333	548.778
20	543.444	550.417	546	552.472

Table 3.10: The local contrast of the original image and the simulation of the 20 microcalcifications of the size group 4 in the 13th projection and the absolute value of the difference.

Particle	Contrast original	Contrast simulation	
1	-0.0076	-0.0049	0.0027
2	-0.0247	-0.0043	0.0204
3	-0.0155	-0.0074	0.0080
4	-0.0036	0.0051	0.0086
5	-0.0010	-0.0016	0.0006
6	-0.0069	-0.0079	0.0010
7	-0.0004	-0.0112	0.0108
8	-0.0108	-0.0132	0.0024
9	0.0057	0.0062	0.0005
10	-0.0125	-0.0063	0.0062
11	-0.0068	-0.0107	0.0039
12	-0.0129	-0.0168	0.0039
13	-0.0081	-0.0181	0.0100
14	-0.0123	-0.0175	0.0053
15	-0.0157	-0.0093	0.0064
16	-0.0173	-0.0172	0.0001
17	-0.0008	-0.0098	0.0091
18	-0.0118	0.0015	0.0134
19	0.0023	-0.0026	0.0050
20	-0.0127	-0.0117	0.0010

Table 3.11: The contrast measurements per size group as absolute values of the average of the 20 contrast evaluations and the average difference in contrast for the 13th projection of the original image and of the simulated image.

Size group	Contrast original	Contrast simulation	Average difference
0	0.0539 ± 0.007204	0.0482 ± 0.007556	0.0078 ± 0.005087
1	0.0352 ± 0.006337	0.0377 ± 0.006018	0.0043 ± 0.004318
2	0.0251 ± 0.007302	0.0259 ± 0.005920	0.0055 ± 0.004268
3	0.0147 ± 0.006280	0.0115 ± 0.006412	0.0056 ± 0.003820
4	0.0087 ± 0.007443	0.0079 ± 0.007175	0.0060 ± 0.005128

CHAPTER 4

Discussion

This thesis aimed at supporting the verification of the novel L2 phantom. This phantom shall be used in quality assessment measurements for digital breast tomography. DBT utilizes X-rays and is especially useful for denser breasts, which suffer from bad detection rates for tumours due to overlapping tissue. The microcalcifications in the phantom of five size groups were investigated as they are one of the test objects in the phantom together with 3D printed non-spiculated mass models. The phantom stands out because of its changeable non-static heterogeneous background. A virtual clinical trial was implemented because of its advantages including decreased cost, more flexibility and less radiation dose. In cooperation with KU Leuven a simulation tool using MATLAB was utilized to simulate the microcalcifications and compare their local contrast to real measurements.

The average difference between 20 contrast measurements of an origianl image with the microcalcifications and a simulation of the particles is equal to 0.0078 ± 0.005087, 0.0043 ± 0.004318, 0.0055 ± 0.004268, 0.0056 ± 0.003820, 0.0060 ± 0.005128 for the size classes 0 to 5. The absolute values of the contrast decrease with decreasing diameter of the microcalcifications. This result is expected as the difference of the feature and the background diminishes as the feature size decreases if the background does not change. The mean pixel value of the particles increases with decreasing diameter. The findings of the standard deviation of the contrast measurements and the average difference suggest uniform data, which is also expected as the same material was used for all size groups and the simulation tool is already verified. The contrast of the simulated particles depend significantly on the input in terms of the MTF and the attenuation. These inputs were already investigated and validated together with the simulation tool.

The biggest difference in contrast is seen for the size class 0. Significant differences in the background can be observed in this size class with the background being smaller for the simulation. The simulation however performs well in terms of the feature values. In the original image of the PMMA the background exhibits a smaller MPV for some of the background ROIs. The particles for class 0 are spread in the y and x-direction

the most of all size groups. It can be concluded that the missmatch in the background MPVs might be to blame for the worse result of the size class 0. On the other hand, the second size group shows the smallest average difference. The smallest standard deviation of the average difference in contrast is found for class 3. The ROIs for these two classes are located in a compact region in the x- and y-direction resulting in more uniform pixel values and less variation in the background MPVs. In general, the standard deviation of the contrast is smaller for the simulation than for the original image. This proposes constant simulation outputs with less variation and also verifies the simulation tool further. The best results are found with ROIs in a small and compact region and size groups with a visible diameter and similar background values in the original and simulation.

For smaller size groups it was increasingly harder to detect the particles and distinguish them from background noise. However, because of the small size, the difference in pixel values of the background and the particles is not as significant for the smaller particles than for the bigger ones. This can be seen in Appendix D: Mean pixel values of the background, where the background values vary for some particles in all five size groups hinting at microcalcifications in close distance altering the background values around the particle. In theory, the background values should be identical for the original and the simulated images. The block of PMMA was not moved between the two acquisitions and the same imaging unit and measurement settings were used. Still, absolute differences up to ten are found for the MPVs of the background ROIs. This suggests the presence of random background noise as well as overlapping and clustering of particles influencing the background measures. This is especially prominant when the contrast is positive. Then the difference of the feature and the background is positive, the pixel value of the feature is bigger than the background.

The randomness of the selection of the particles should oppose the dilemma of false classification. However, the smallest particles have a mean diameter of 0.1325 mm. As the pixel size is 0.085 mm according to the DICOM tag (0028,0030) the microcalcifications of this size group measure only 1.5 pixels, which makes them hard to distinguish and might lead to inaccurate detection of particles. Still, the average difference is significantly small considering the unknown locations of the microcalcifications and justifies the use of the material in the phantom as their depiction is the same as for the verified simulations. This virtual clinical trial was successful and showed that the contrast of the microcalcifications in the phantom are imaged in DBT images sufficiently equally to the already tested and verified simulation, while the significance of microcalcifications in the clinical diagnosis of breast cancer was already described in foregone research papers.

Considering additional research examining contrast measurements, the paper [49] comes to mind. It verifies the used simulation tool and utilizes an aluminium plate to measure the contrast. However, this study focused more on different tube settings using the same particle for all measurements. The conclusion was a successful verification of the simulation tool with contrast calculations of the simulation and the original image differing in the third decimal number. Similar results were found in this thesis supporting

the claim of a successful depiction of the contrast of the microcalcification in the phantom in DBT images.

Concerning the simulation tool it should be stated that the particles are lying on top of the 4 cm of PMMA in the original image. However, the simulation itself stops at 4 cm height and is not able to simulate particles on top of the surrounding volume. Hence, it was recommended by KU Leuven to choose 2 cm as the z-position for the simulation. Test simulations supported this proposal as no significant difference in pixel values was found for the microparticles with different z-positions. It is suggested to further improve the tool and make simulations on top of the volume possible. This would make the resulting simulations even more close to the real tomosynthesis image. Furthermore, the mean was taken for the diameter of each size class. However, the particles are not all the same size. Their diameter might range from the minimum and maximum value of the size intervals. One suggestion would be to simulate microcalcifications with a random size in the given size range per class. This would potentially improve the results to be more alike the original image.

Connected to the last point, the composition of the original image should also be noted. The particles were spread across the PMMA without any systematical arrangement. In the phantom, the particles are arranged in a set manner with coherent distances between the particles and an arrangement in a pentagon with a central particle. Because of the randomness of the particles' positions in the test image, which was taken by another employee of the Medical University of Vienna, it cannot be ensured, that there is no overlapping of particles or clusters of microcalcifications. Further, the results for class 0 suggest that a larger distance between the particles resulted in larger differences in background values. In the L2 phantom, the particles are picked and attached to the plate inside the casing one at a time by hand assuring consistent results. In retrospect, the particles could have also been placed on the PMMA block individually and at known positions for this trial, in order to ensure accurate detection of the microcalcifications and an increase of the accuracy of the results as this approach is also more similar to the manufacturing process of the phantom.

For the purpose of evaluating the perceptibility of the microcalcifications, a detectability test using human readers is planned for the future. This will include the comparison of the detection rates of the real microcalcifications in the phantom to simulations of the particles in patient images, taking into consideration the non-uniform background of images taken in clinical settings, which is different to the uniform background of the used PMMA block. Consequently, the use of micorcalcifications in the L2 phantom can be justified even more and the results are planned to be published in a paper together with the contrast evaluation of this thesis. As one of the last steps to fully investigate and evaluate the novel phantom, contrast and detectability tests with the same setup and steps shall be done for the mass models in the phantom in the future.

CHAPTER 5

Conclusion

To sum up, one of the used materials in a novel phantom for quality assurance in mammography was validated. In order to do so the contrast of microcalcifications taken on a bare plastic block were compared to simulations done with a verified simulation tool. If the local contrast of an image of the material is sufficiently similar to the simulation, then the use of the microcalcifications in the phantom is justified.

The found results for the average difference in contrast of the simulated and the original image range from 0.0043 to 0.0078. Because the particles were spread on the plastic block randomly, clustering of particles and on the contrary large distances between the particles and differences in the 4 background ROIs can be seen. Moreover, it was hard to detect the particles of the smallest size group by eye, as they were only 1.5 pixels big and hard to distinguish from background noise. It is suggested that fixation of the particles one by one in set positions would result in better matches of the contrast values.

This study was the first step in the evaluation of the materials in the novel L2 phantom. As the contrast was evaluated in this thesis, in future tests the detectability of the microcalcifications will the assessed and published in a paper together with the results of the contrast comparison. This time, simulations will be compared with acquisitions of the phantom. As the simulation tool has not been assessed for calcium carbonate, this work is also support for the ability of the simulation tool. Regarding the phantom, the significantly small average difference in contrast and the small standard deviations suggest that the particles are presented in the mammography images correctly and similarly to the simulations. Hence, the use of this material in quality assurance is valid. This validity will be further studied with the detectability test.

This study was limited due to the used simulation tool. It is only able to simulate materials with one set diameter into a volume. This workflow was not optimal for the size groups, whose diameters ranged from a minimum to a maximum value. Furthermore, the particles are placed on top of a block of PMMA in the original image. Yet, the

simulation tool is not able to place particles outside the base volume. Due to these two restraints, the mean diameter was used for each size groups of the microcalcifications and the spheres were placed inside the volume. Improvements to the simulation tool should lead to more accurate results.

Building on the promising results of this virtual clinical trial to evaluate the contrast of the microcalcifications in the L2 phantom, the non-spiculated masses, which are the second test object in the phantom, will be further investigated. Due to the L2 phantom having a variable and non-uniform background and DBT showing better detection rates especially in denser breasts where overlapping tissue might mask or mimic tumours, the combination of both hints at better and earlier detection of breast tumours with improved image quality control tests. The found average difference in contrast is significantly small to support the use of the microcalcifications in the phantom. A detectability test of the particles conducted in the future will additionally explore this material together with the phantom's non-uniform background.

List of Figures

List of Tables

List of Abbreviations

2D	2-dimensional
3D	3-dimensional
AAPM	American Association of Physicists in Medicine
ACR	American College of Radiology
AGES	Austrian Agency for Health and Food Safety (Österreichische Agentur für Gesundheit und Ernährungssicherheit)
BP	Back-projection
CDMAM	Contrast detail mammography
CNR	Contrast-to-noise ration
DBT	Digital breast tomography
DICOM	Digital Imaging and Communications in Medicine
DQE	Detective quantum efficiency
EUREF	European Reference Organisation for Quality Assured Breast Screening and Diagnostic Services
FBP	Filtered back-projection
FFDM	Full-field digital mammography
LSF	Line spread function
MPV	Mean pixel value
MTF	Modular transfer function
NPS	Noise power spectrum
PACS	Picture archive and communication system
PMMA	Polymethylmethacrylate
ROI	Region of interest
SDNR	Signal-difference-to-noise ratio
SNR	Signal-to-noise ratio
SPR	Scatter-to-primary ratio
TFT	Thin film transistor
VBD	Volumetric breast density
VCT	Virtual clinical trial

Bibliography

[1] EUROPA DONNA. *Breast Cancer Facts*. 2018. URL: https://www.europadonna.org/breast-cancer-facs/ (visited on 02/14/2022).

[2] APA/Red. *42.000 Krebserkrankungen und 20.000 Tote pro Jahr in Österreich*. vienna.at. Jan. 27, 2022. URL: https://www.vienna.at/42-000-krebserkrankungen-und-20-000-tote-pro-jahr-in-oesterreich/7272027 (visited on 02/14/2022).

[3] European Society for Medical Oncology. *Cancer Mortality Predictions for the 10 Major Causes of Cancer Mortality and Total Cancer in 2022 in the European Union*. Feb. 25, 2022. URL: https://www.esmo.org/oncology-news/cancer-mortality-predictions-for-the-10-major-causes-of-cancer-mortality-and-total-cancer-in-2022-in-the-european-union (visited on 04/19/2022).

[4] European Union. *2020 Cancer incidence and mortality in EU-27 countries*. EU Science Hub - European Commission. July 22, 2020. URL: https://joint-research-centre.ec.europa.eu/jrc-news/2020-cancer-incidence-and-mortality-eu-27-countries-2020-07-22_en (visited on 02/14/2022).

[5] Breastcancer.org. *Breast Cancer Facts and Statistics*. Mar. 10, 2022. URL: https://www.breastcancer.org/facts-statistics (visited on 04/19/2022).

[6] National Cancer Institute at the National Institutes of Health. *breast cancer*. URL: https://www.cancer.gov/publications/dictionaries/cancer-terms/def/breast-cancer (visited on 02/14/2022).

[7] Centers for Disease Control & Prevention and Division of Cancer Prevention & Control. *What Is Breast Cancer?* Sept. 22, 2021. URL: https://www.cdc.gov/cancer/breast/basic_info/what-is-breast-cancer.htm (visited on 02/14/2022).

[8] American Cancer Society. *Types of Breast Cancer*. Nov. 19, 2021. URL: https://www.cancer.org/cancer/breast-cancer/about/types-of-breast-cancer.html (visited on 02/14/2022).

[9] MAMMOGUIDE. *Excise It*. 2020. URL: https://www.mammoguide.com/excise-it-high-risk-breast-lesions.html (visited on 02/14/2022).

[10] J Louise Jones. “Breast”. In: *Underwood’s Pathology*. 7th edition. Elseviert Ltd., 2019, pp. 416–437.

[11] Rachel F. Cox and Maria P. Morgan. “Microcalcifications in breast cancer: Lessons from physiological mineralization”. In: *Bone* 53.2 (2013), pp. 437–450. DOI: 10.1016/j.bone.2013.01.013.

[12] P. Henrot et al. “Breast microcalcifications: The lesions in anatomical pathology”. In: *Diagnostic and Interventional Imaging* 95.2 (2014), pp. 141–152. DOI: 10.1016/j.diii.2013.12.011.

[13] American Cancer Society. *Breast Cancer Facts & Figures 2019-2020*. 2019. URL: https://www.cancer.org/content/dam/cancer-org/research/cancer-facts-and-statistics/breast-cancer-facts-and-figures/breast-cancer-facts-and-figures-2019-2020.pdf (visited on 02/14/2022).

[14] American Cancer Society. *Cancer Facts & Figures 2022*. 2022. URL: https://www.cancer.org/content/dam/cancer-org/research/cancer-facts-and-statistics/annual-cancer-facts-and-figures/2022/2022-cancer-facts-and-figures.pdf (visited on 02/14/2022).

[15] Bundesministerium für Soziales, Gesundheit, Pflege und Konsumentenschutz. *Screening-Programm: Brustkrebs-Früherkennung*. Sept. 1, 2021. URL: https://www.oesterreich.gv.at/themen/gesundheit_und_notfaelle/medizinische_versorgung/screening-programm_brustkrebs-frueherkennung.html (visited on 02/14/2022).

[16] L Cockmartin et al. “Design and application of a structured phantom for detection performance comparison between breast tomosynthesis and digital mammography”. In: *Phys. Med. Biol.* 62.3 (2017), pp. 758–780. DOI: 10.1088/1361-6560/aa5407.

[17] Nieun Seo et al. “Digital breast tomosynthesis versus full-field digital mammography: comparison of the accuracy of lesion measurement and characterization using specimens”. In: *Acta Radiol* 55.6 (2014), pp. 661–667. DOI: 10.1177/0284185113503636.

[18] Elisabeth Salomon et al. “Equivalent breast thickness and dose sensitivity of a next iteration 3D structured breast phantom with lesion models”. In: *Medical Imaging 2020: Physics of Medical Imaging*. Vol. 11312. International Society for Optics and Photonics, 2020. DOI: 10.1117/12.2548956.

[19] Mirjan M. Nadrljanski. *Anode (x-ray tube)*. Radiopaedia. Jan. 17, 2010. DOI: 10.53347/rID-8178.

[20] Martin Berger, Qiao Yang, and Andreas Maier. “X-ray Imaging”. In: *Medical Imaging Systems: An Introductory Guide*. Ed. by Andreas Maier et al. Cham (CH): Springer, 2018. Chap. 7. ISBN: 978-3-319-96519-2 978-3-319-96520-8.

[21] Perry Sprawls. *Mammography Physics and Technology for effective clinical imaging*. URL: http://www.sprawls.org/resources/MAMMO/module.htm#15 (visited on 03/04/2022).

[22] International Atomic Energy Agency. *Diagnostic Radiology Physics: A Handbook for Teachers and Students*. Vienna, 2014. ISBN: 978–92–131010–1.

[23] Suman Shrestha, Srinivasan Vedantham, and Andrew Karellas. "Towards Standardization of X-ray Beam Filters in Digital Mammography and Digital Breast Tomosynthesis: Monte Carlo simulations and analytical modelling". In: *Phys Med Biol* 62.5 (Mar. 7, 2017), pp. 1969–1993. DOI: 10.1088/1361-6560/aa58c8.

[24] Zemar Vajuhudeen. *K-absorption edge*. Radiopaedia. July 1, 2020. DOI: 10.53347/rID-79625.

[25] National Institute of Biomedical Imaging & Bioengineering. *X-rays*. URL: https://www.nibib.nih.gov/science-education/science-topics/x-rays (visited on 03/03/2022).

[26] Jerrold T. Bushberg et al. *The Essential Physics of Medical Imaging*. Ed. by Charles W. Mitchell. Philadelphia: Lippincott Williams & Wilkins, 2012. ISBN: 978-0-7817-8057-5.

[27] Michael Burch et al. *X-Ray Imaging: Fundamentals*. Radiology Key. Apr. 17, 2020. URL: https://radiologykey.com/x-ray-imaging-fundamentals/ (visited on 03/06/2022).

[28] Mark Hammer. *X-Ray Physics: X-Ray Interaction with Matter and Attenuation*. 2014. URL: http://xrayphysics.com/attenuation.html (visited on 03/06/2022).

[29] Francesco Priamo and Andrea Sangheli. *Linear attenuation coefficient*. Radiopaedia. Nov. 5, 2014. DOI: 10.53347/rID-31918.

[30] SUNY Upstate Medical University. *Scatter Removal Grids*. 1988-2022. URL: https://www.upstate.edu/radiology/education/rsna/radiography/scattergrid.php (visited on 03/13/2022).

[31] Elena Salvagnini et al. "Quantification of scattered radiation in projection mammography: Four practical methods compared: Scatter in mammography". In: *Med. Phys.* 39.6 (May 15, 2012), pp. 3167–3180. DOI: 10.1118/1.4711754.

[32] Da Zhang, Xinhua Li, and Bob Liu. "Multi-resolution analysis of scatter in digital breast tomosynthesis imaging". In: SPIE Medical Imaging. Ed. by Robert M. Nishikawa and Bruce R. Whiting. Lake Buena Vista (Orlando Area), Florida, USA, Mar. 6, 2013, p. 86685L. DOI: 10.1117/12.2007315.

[33] George Zentai. "Contrast Enhancement in Mammography Imaging Including K Edge Filtering". In: *Imaging of the Breast - Technical Aspects and Clinical Implication*. Ed. by Laszlo Tabar. InTech, Mar. 16, 2012, pp. 133–158. DOI: 10.5772/31622.

[34] William R. Geiser, Samuel A. Einstein, and Wei-Tse Yang. "Artifacts in Digital Breast Tomosynthesis". In: *American Journal of Roentgenology* 211.4 (Oct. 2018), pp. 926–932. DOI: 10.2214/AJR.17.19271.

[35] Ayush Goel. *Kilovoltage peak*. Radiopaedia. June 11, 2014. DOI: 10.53347/rID-29650.

[36] Sarah Abdulla. *Production of X-rays*. Oct. 10, 2021. URL: https://www.radiologycafe.com/frcr-physics-notes/x-ray-imaging/production-of-x-rays/ (visited on 03/04/2022).

[37] Jeremy Jones. *Absorbed dose*. Radiopaedia. Dec. 4, 2008. DOI: 10.53347/rID-5097.

[38] Edward R. Hendrick and Debra M. Ikeda. *Mammography Acquisition: Screen-Film and Digital Mammography, the Mammography Quality Standards Act, and Computer-Aided Detection*. June 12, 2015. URL: https://clinicalgate.com/mammography-acquisition-screen-film-and-digital-mammography-the-mammography-quality-standards-act-and-computer-aided-detection/ (visited on 03/19/2022).

[39] Euclid Seeram. "Full-Field Digital Mammography". In: *Digital Radiography*. Singapore: Springer Singapore, 2019, pp. 111–123. DOI: 10.1007/978-981-13-3244-9_7.

[40] Redaktion Gesundheitsportal. *Brustkrebs: Diagnose*. Bundesministerium für Soziales, Gesundheit, Pflege und Konsumentenschutz. Apr. 21, 2022. URL: https://www.gesundheit.gv.at/krankheiten/krebs/brustkrebs/mammographie-ultraschall (visited on 05/09/2022).

[41] Margarita Chevalier et al. "Image Quality Requirements for Digital Mammography in Breast Cancer Screening". In: *Imaging of the Breast - Technical Aspects and Clinical Implication*. Ed. by Laszlo Tabar. InTech, 2012, pp. 115–132. ISBN: 978-953-51-0284-7.

[42] Elisabeth Salomon. "Phantome zur Bestimmung der Bildgüte in der Tomosynthese". Online seminar. ÖGMP Fortbildung, Mar. 18, 2021.

[43] Donella Puliti et al. "Volumetric breast density and risk of advanced cancers after a negative screening episode: a cohort study". In: *Breast Cancer Res* 20.1 (Dec. 2018), p. 95. DOI: 10.1186/s13058-018-1025-8.

[44] A Oliver. "Evaluating automated density maps for local breast density assessment". In: *DI Europe* (Oct. 2017), pp. 56–58. URL: https://www.dieurope.com/pdf/application.php?ID=134984 (visited on 02/23/2022).

[45] Elsevier B.V. *Fibroglandular Tissue*. 2022. URL: https://www.sciencedirect.com/topics/engineering/fibroglandular-tissue (visited on 03/19/2022).

[46] Katharina Holland et al. “Quantification of masking risk in screening mammography with volumetric breast density maps”. In: *Breast Cancer Res Treat* 162.3 (Apr. 2017), pp. 541–548. DOI: 10.1007/s10549-017-4137-4.

[47] Y Faridah. “Digital versus screen film mammography: a clinical comparison”. In: *Biomed Imaging Interv J* 4.4 (Oct. 1, 2008), e31. DOI: 10.2349/biij.4.4.e31.

[48] Etta D. Pisano and Martin J. Yaffe. “Digital Mammography”. In: *Radiology* 234.2 (Feb. 2005), pp. 353–362. DOI: 10.1148/radiol.2342030897.

[49] Liesbeth Vancoillie et al. “Verification of the accuracy of a hybrid breast imaging simulation framework for virtual clinical trial applications”. In: *J Med Imaging* 7.4 (2020), p. 042804. DOI: 10.1117/1.JMI.7.4.042804.

[50] Mehran Ebrahimi. “Breast Imaging: Mammography, Digital Tomosynthesis, Dynamic Contrast Enhancement”. In: *Encyclopedia of Biomedical Engineering*. Elsevier, 2019, pp. 501–504. ISBN: 978-0-12-805144-3. DOI: 10.1016/B978-0-12-801238-3.99943-4.

[51] Premkumar Elangovan et al. “Development and validation of a modelling framework for simulating 2D-mammography and breast tomosynthesis images”. In: *Phys. Med. Biol.* 59.15 (Aug. 7, 2014), pp. 4275–4293. DOI: 10.1088/0031-9155/59/15/4275.

[52] John W. Garrett et al. “Reduced anatomical clutter in digital breast tomosynthesis with statistical iterative reconstruction”. In: *Med Phys* 45.5 (May 2018), pp. 2009–2022. DOI: 10.1002/mp.12864.

[53] Ioannis Sechopoulos. “A review of breast tomosynthesis. Part I. The image acquisition process”. In: *Med. Phys.* 40.1 (Jan. 2013), p. 014301. DOI: 10.1118/1.4770279.

[54] Ioannis Sechopoulos. “A review of breast tomosynthesis. Part II. Image reconstruction, processing and analysis, and advanced applications”. In: *Med Phys* 40.1 (Jan. 2013), p. 014302. DOI: 10.1118/1.4770281.

[55] Tao Wu et al. “A comparison of reconstruction algorithms for breast tomosynthesis”. In: *Med. Phys.* 31.9 (Aug. 26, 2004), pp. 2636–2647. DOI: 10.1118/1.1786692.

[56] Yiheng Zhang et al. “A comparative study of limited-angle cone-beam reconstruction methods for breast tomosynthesis”. In: *Medical Physics* 33.10 (2006), pp. 3781–3795. DOI: 10.1118/1.2237543.

[57] Jasmina Ludwig et al. “A Novel Approach for Filtered Backprojection in Tomosynthesis Based on Filter Kernels Determined by Iterative Reconstruction Techniques”. In: *Proceedings of the 9th International Workshop on Digital Mammography*. IWDM ’08. Tucson, AZ, USA: Springer-Verlag, 2008, pp. 612–620. ISBN: 9783540705376. DOI: 10.1007/978-3-540-70538-3_85.

[58] International Atomic Energy Agency (IAEA). *3D image reconstruction*. 2016. URL: https://humanhealth.iaea.org/HHW/MedicalPhysics/NuclearMedicine/ImageAnalysis/3Dimagereconstruction/index.html (visited on 03/21/2022).

[59] Hugo de las Heras et al. "A phantom using titanium and Landolt rings for image quality evaluation in mammography". In: *Phys. Med. Biol.* 58.8 (2013), pp. L17–L30. DOI: 10.1088/0031-9155/58/8/L17.

[60] Referenzzentrum Mammographie SüdWest. *SDNR-Berechnung*. 2022. URL: https://referenzzentrum-suedwest.de/qualitaetssicherung-mammographie-screening/physikalisch-technische-qualitaetssicherung/sdnr-rechner (visited on 02/17/2022).

[61] AGES RefZQS. *Anleitung für die Durchführung von Tests an Mammografie- und Peripheriesystemen laut EUREF-Ö*. 2021. URL: https://www.ages.at/download/sdl-eyJ0eXAiOiJKV1QiLCJhbGciOiJIUzI1NiJ9.eyJpYXQiOjE2MDk0NTkyMDAsImV4cCI6NDA3MDkwODgwMCwidXNlciI6MCwiZ3JvdXBzIjpbMCwtMV0sImZpbGUiOiJmaWxlYWRtaW5cL0FHRVNfMjAyMlwvVU1XRUxUXC9SYWRpb2FrdGl2aXRcdTAwZTR0XC9UZWNobmlzY2hlX1F1YWxpdFx1MDBlNHRzc2ljaGVydW5nX2ltX0JydXN0a3JlYnMtRnJcdTAwZmNoZXJrZW5udW5nc3Byb2dyYW1tXC9MXzg5OTVfNV9BbmxlaXR1bmctQVQtSlQtSFQucGRmIiwicGFnZSI6MTkwOX0.6mg2rTDGtdXk7s0OEU5MP4NsDxkcgTMfR8pnC-mzWS0/L_8995_5_Anleitung-AT-JT-HT.pdf (visited on 02/17/2022).

[62] U.S. Food and Drug Administration. *Phantoms*. Feb. 12, 2017. URL: https://www.fda.gov/radiation-emitting-products/nationwide-evaluation-x-ray-trendsnext/phantoms (visited on 02/17/2022).

[63] N. W. Marshall et al. "Image quality assessment in digital mammography: part I. Technical characterization of the systems". In: *Phys. Med. Biol.* 56.14 (2011), pp. 4201–4220. DOI: 10.1088/0031-9155/56/14/002.

[64] Jerry A. Thomas et al. "Contrast-detail phantom scoring methodology: Contrast-detail phantom scoring methodology". In: *Med. Phys.* 32.3 (2005), pp. 807–814. DOI: 10.1118/1.1862097.

[65] Anant Agrawal et al. "Regulatory perspectives and research activities at the FDA on the use of phantoms with in vivo diagnostic devices". In: *Design and Performance Validation of Phantoms Used in Conjunction with Optical Measurements of Tissue*. SPIE Proceedings. Ed. by Robert J. Nordstrom. Vol. 6870. 2008, p. 687005. DOI: 10.1117/12.768537.

[66] Computerized Imaging Reference Systems. *ACR Digital Mammography Phantom*. 2022. URL: https://www.cirsinc.com/products/mammography/acr-digital-mammography-phantom/ (visited on 02/17/2022).

[67] Österreichische Agentur für Gesundheit und Ernährungssicherheit GmbH. *Strahlenschutz Serviceleistungen*. May 5, 2022. URL: https://www.ages.at/umwelt/radioaktivitaet/strahlenschutz-serviceleistungen (visited on 05/09/2022).

[68] Lynda C. Ikejimba et al. "A four-alternative forced choice (4AFC) methodology for evaluating microcalcification detection in clinical full-field digital mammography (FFDM) and digital breast tomosynthesis (DBT) systems using an inkjet-printed anthropomorphic phantom". In: *Medical Physics* 46.9 (2019), pp. 3883–3892. DOI: 10.1002/mp.13629.

[69] F. di Franco et al. "GEANT4 Monte Carlo simulations for virtual clinical trials in breast X-ray imaging: Proof of concept". In: *Physica Medica* 74 (June 2020), pp. 133–142. DOI: 10.1016/j.ejmp.2020.05.007.

[70] Ehsan Abadi et al. "Virtual clinical trials in medical imaging: a review". In: *J Med Imaging (Bellingham)* 7.4 (July 2020), p. 042805. DOI: 10.1117/1.JMI.7.4.042805.

[71] Jun Wei et al. "Synthesizing mammogram from digital breast tomosynthesis". In: *Phys. Med. Biol.* 64.4 (Feb. 11, 2019), p. 045011. DOI: 10.1088/1361-6560/aafcda.

[72] Carsten Leinweber, Joscha Maier, and Marc Kachelrieß. "X-ray spectrum estimation for accurate attenuation simulation". In: *Med. Phys.* 44.12 (Dec. 2017), pp. 6183–6194. DOI: 10.1002/mp.12607.

[73] The MathWorks. *Neues Release 2013b der MATLAB- und Simulink Produktfamilien von MathWorks*. Sept. 6, 2013. URL: https://de.mathworks.com/company/newsroom/mathworks-announces-release-2013b-of-the-matlab-and-simulink-product-families.html (visited on 12/17/2021).

[74] Microsoft. *Microsoft Excel*. 2021. URL: https://www.microsoft.com/de-at/microsoft-365/excel (visited on 12/17/2021).

[75] USA National Institutes of Health. *ImageJ*. Nov. 28, 2018. URL: https://imagej.nih.gov/ij/index.html (visited on 12/17/2021).

Appendix A: Positions of the particle measurements

Positions ROIs Particles Class 0			Positions ROIs Particles Class 1		
Particle	X	Y	Particle	X	Y
1	191.718	245.013	1	199.708	197.668
2	193.758	238.893	2	196.393	194.268
3	197.923	239.403	3	197.243	195.118
4	202.938	224.018	4	191.803	195.713
5	202.258	224.868	5	194.438	190.018
6	199.368	241.613	6	194.013	188.148
7	199.708	238.383	7	196.818	184.663
8	198.348	249.093	8	194.523	184.918
9	196.138	229.033	9	197.328	193.588
10	196.138	254.533	10	192.993	193.928
11	197.923	247.223	11	195.798	192.228
12	196.393	243.398	12	198.093	185.343
13	194.353	257.678	13	192.543	182.453
14	197.498	234.643	14	193.248	184.493
15	197.158	240.253	15	192.738	191.208
16	196.733	238.978	16	195.033	185.768
17	197.668	236.428	17	194.183	195.033
18	199.538	248.073	18	195.543	180.838
19	194.948	243.653	19	194.098	183.473
20	199.283	247.053	20	193.758	182.453

Positions ROIs Particles Class 2			Positions ROIs Particles Class 3		
Particle	X	Y	Particle	X	Y
1	190.103	151.853	1	198.858	99.238
2	192.993	150.493	2	197.583	101.448
3	193.758	151.768	3	197.328	101.023
4	190.698	149.983	4	197.668	94.903
5	192.228	149.472	5	198.433	92.693
6	193.078	149.303	6	199.198	103.573
7	195.883	150.153	7	196.818	102.978
8	195.713	150.663	8	194.268	100.428
9	189.593	148.282	9	195.373	102.128
10	190.443	155.508	10	196.053	101.533
11	189.763	156.188	11	194.353	92.778
12	194.778	153.723	12	194.863	95.073
13	188.488	154.318	13	200.048	99.833
14	189.168	153.723	14	198.178	97.793
15	190.443	153.978	15	187.893	96.943
16	191.208	154.403	16	191.973	96.518
17	190.613	145.138	17	194.013	96.858
18	188.062	146.243	18	196.138	98.558
19	188.573	147.433	19	196.733	96.943
20	193.673	152.788	20	191.718	98.048

Positions ROIs Particles Class 4

Particle	X	Y
1	197.073	54.273
2	195.628	54.698
3	196.053	56.313
4	196.818	56.568
5	196.818	51.723
6	195.713	53.168
7	196.223	50.023
8	195.203	50.958
9	195.543	48.323
10	193.758	55.633
11	198.518	54.188
12	197.583	51.638
13	195.203	49.853
14	193.248	48.493
15	192.993	50.363
16	190.103	51.383
17	190.188	50.448
18	191.208	49.683
19	192.143	48.833
20	189.933	53.763

Appendix B: Positions of the background measurements

Positions ROIs Background Class 0

Particle	ROI 1 X	ROI 1 Y	ROI 2 X	ROI 2 Y	ROI 3 X	ROI 3 Y	ROI 4 X	ROI 4 Y
1	192.143	245.013	191.718	244.588	191.718	245.438	191.293	245.013
2	194.183	238.893	193.758	238.468	193.333	238.893	193.758	239.318
3	197.923	238.978	198.348	239.403	197.923	239.828	197.498	239.403
4	203.363	224.018	202.938	223.593	202.938	224.443	202.513	224.018
5	202.258	224.443	202.683	224.868	202.258	225.293	201.833	224.868
6	199.793	241.613	199.368	241.188	198.943	241.613	199.368	242.038
7	199.708	237.958	200.133	238.383	199.708	238.808	199.283	238.383
8	198.773	249.093	198.348	248.668	198.348	249.518	197.923	249.093
9	196.562	229.033	196.138	228.608	195.713	229.033	196.138	229.458
10	196.562	254.533	196.138	254.108	196.138	254.958	195.713	254.533
11	198.348	247.223	197.923	246.798	197.923	247.648	197.498	247.223
12	196.818	243.398	196.393	242.973	196.393	243.823	195.968	243.398
13	194.778	257.678	194.353	257.252	194.353	258.103	193.928	257.678
14	197.923	234.643	197.498	234.218	197.498	235.068	197.073	234.643
15	197.583	240.253	197.158	239.828	197.158	240.678	196.733	240.253
16	196.733	238.553	197.158	238.978	196.733	239.403	196.308	238.978
17	198.093	236.428	197.668	236.003	197.668	236.853	197.243	236.428
18	199.963	248.073	199.538	247.648	199.538	248.498	199.113	248.073
19	195.373	243.653	194.948	243.228	194.948	244.078	194.523	243.653
20	199.708	247.053	199.283	247.478	199.283	246.628	198.858	247.053

Positions ROIs Background Class 1

Particle	ROI1 X	ROI1 Y	ROI2 X	ROI2 Y	ROI3 X	ROI3 Y	ROI4 X	ROI4 Y
1	199.708	197.243	200.133	197.668	199.708	198.093	199.283	197.668
2	196.393	193.843	196.818	194.268	196.393	194.693	195.968	194.268
3	197.243	194.693	197.668	195.118	197.243	195.543	196.818	195.118
4	191.803	195.288	192.228	195.713	191.803	196.138	191.378	195.713
5	194.438	189.593	194.863	190.018	194.438	190.358	194.013	190.018
6	194.013	187.723	194.438	188.148	194.013	188.573	193.588	188.148
7	196.818	184.238	197.243	184.663	196.818	185.088	196.393	184.663
8	194.523	184.493	194.948	184.918	194.523	185.343	194.098	184.918
9	197.328	193.163	197.753	193.588	197.328	194.013	196.903	193.588
10	192.993	193.503	193.418	193.928	192.993	194.353	192.568	193.928
11	195.798	191.803	196.223	192.228	195.798	192.653	195.373	192.228
12	198.093	184.918	198.518	185.343	198.093	185.768	197.668	185.343
13	195.543	182.028	195.968	182.453	195.543	182.878	195.118	182.453
14	193.248	184.068	193.673	184.493	193.248	184.918	192.823	184.493
15	192.738	190.783	193.163	191.208	192.738	191.633	192.312	191.208
16	195.033	185.343	195.458	185.768	195.033	186.193	194.608	185.768
17	194.183	194.608	194.608	195.033	194.183	195.458	193.758	195.033
18	195.543	180.413	195.968	180.838	195.543	181.178	195.118	180.838
19	194.098	183.048	194.523	183.473	194.098	183.812	193.673	183.473
20	193.758	182.028	194.183	182.453	193.758	182.878	193.333	182.453

Positions ROIs Background Class 2

Particle	ROI1 X	ROI1 Y	ROI2 X	ROI2 Y	ROI3 X	ROI3 Y	ROI4 X	ROI4 Y
1	190.528	151.853	190.103	152.278	189.678	151.853	190.103	151.428
2	193.418	150.493	192.993	150.918	192.568	150.493	192.993	150.068
3	194.183	151.768	193.758	152.193	193.333	151.768	193.758	151.343
4	191.123	149.983	190.698	150.407	190.273	149.983	190.698	149.558
5	192.653	149.472	192.228	149.898	191.803	149.472	192.228	149.048
6	193.503	149.303	193.078	149.728	192.653	149.303	193.078	148.877
7	196.308	150.153	195.883	150.578	195.458	150.153	195.883	149.728
8	196.138	150.663	195.713	151.088	195.288	150.663	195.713	150.238
9	189.593	147.858	190.018	148.282	189.593	148.708	189.168	148.282
10	190.443	155.083	190.868	155.508	190.443	155.933	190.018	155.508
11	190.188	156.188	189.763	156.613	189.338	156.188	189.763	155.763
12	195.203	153.723	194.778	154.148	194.353	153.723	194.778	153.298
13	188.913	154.318	188.488	154.743	188.062	154.318	188.488	153.893
14	189.593	153.723	189.168	154.148	188.743	153.723	189.168	153.298
15	190.868	153.978	190.443	154.403	190.018	153.978	190.443	153.553
16	191.633	154.403	191.208	154.828	190.783	154.403	191.208	153.978
17	191.038	145.138	190.613	145.562	190.188	145.138	190.613	144.713
18	188.488	146.243	188.062	146.668	187.638	146.243	188.062	145.818
19	188.998	147.433	188.573	147.858	188.148	147.433	188.573	147.008
20	194.098	152.788	193.673	153.213	193.248	152.788	193.673	152.363

Positions ROIs Background Class 3

Particle	ROI1 X	ROI1 Y	ROI2 X	ROI2 Y	ROI3 X	ROI3 Y	ROI4 X	ROI4 Y
1	199.283	99.238	198.858	99.663	198.433	99.238	198.858	98.812
2	198.008	101.448	197.583	101.873	197.158	101.448	197.583	101.023
3	197.753	101.023	197.328	101.448	196.903	101.023	197.328	100.598
4	198.093	94.903	197.668	95.328	197.243	94.903	197.668	94.478
5	198.858	92.693	198.433	93.118	198.008	92.693	198.433	92.268
6	199.623	103.573	199.198	103.998	198.773	103.573	199.198	103.148
7	197.243	102.978	196.818	103.403	196.393	102.978	196.818	102.553
8	194.693	100.428	194.268	100.853	193.843	100.428	194.268	100.003
9	195.798	102.128	195.373	102.553	194.948	102.128	195.373	101.703
10	196.478	101.533	196.053	101.958	195.628	101.533	196.053	101.108
11	194.778	92.778	194.353	93.203	193.928	92.778	194.353	92.353
12	195.288	95.073	194.863	95.498	194.438	95.073	194.863	94.648
13	200.473	99.833	200.048	100.258	199.623	99.833	200.048	99.408
14	198.603	97.793	198.178	98.218	197.753	97.793	198.178	97.368
15	188.318	96.943	187.893	97.368	187.468	96.943	187.893	96.518
16	192.398	96.518	191.973	96.943	191.548	96.518	191.973	96.093
17	194.438	96.858	194.013	97.283	193.588	96.858	194.013	96.433
18	196.562	98.558	196.138	98.983	195.713	98.558	196.138	98.133
19	197.158	96.943	196.733	97.368	196.308	96.943	196.733	96.518
20	192.143	98.048	191.718	98.473	191.293	98.048	191.718	97.623

Positions ROIs Background Class 4

Particle	ROI1 X	ROI1 Y	ROI2 X	ROI2 Y	ROI3 X	ROI3 Y	ROI4 X	ROI4 Y
1	197.498	54.273	197.073	54.698	196.648	54.273	197.073	53.848
2	196.053	54.698	195.628	55.123	195.203	54.698	195.628	54.273
3	196.478	56.313	196.053	56.738	195.628	56.313	196.053	55.888
4	197.243	56.568	196.818	56.993	196.393	56.568	196.818	56.143
5	197.243	51.723	196.818	52.148	196.393	51.723	196.818	51.298
6	196.138	53.168	195.713	53.593	195.288	53.168	195.713	52.743
7	196.648	50.023	196.223	50.448	195.798	50.023	196.223	49.598
8	195.628	50.958	195.203	51.383	194.778	50.958	195.203	50.533
9	195.968	48.323	195.543	48.748	195.118	48.323	195.543	47.898
10	194.183	55.633	193.758	56.058	193.333	55.633	193.758	55.208
11	198.943	54.188	198.518	54.613	198.093	54.188	198.518	53.763
12	198.008	51.638	197.583	52.063	197.158	51.638	197.583	51.213
13	195.628	49.853	195.203	50.278	194.778	49.853	195.203	49.428
14	193.673	48.493	193.248	48.918	192.823	48.493	193.248	48.068
15	193.418	50.363	192.993	50.788	192.568	50.363	192.993	49.938
16	190.528	51.383	190.103	51.808	189.678	189.678	190.103	50.958
17	190.613	50.448	190.188	50.873	189.763	50.448	190.188	50.023
18	191.633	49.683	191.208	50.108	190.783	49.683	191.208	49.258
19	192.568	48.833	192.143	49.258	191.718	48.833	192.143	48.408
20	190.358	53.763	189.933	54.188	189.508	53.763	189.933	53.338

Appendix C: X- and y-coordinates for the simulation

Simulation Inputs Class 0			Simulation Inputs Class 1		
Particle	X	Y	Particle	X	Y
1	74.60523077	-88.70774207	1	82.165	-43.9925113041
2	76.53538462	-82.91728053	2	79.02376923	-40.77558823
3	80.47138462	-83.399819	3	79.828	-41.579819
4	85.22107692	-68.8385113	4	74.68092308	-42.13804977
5	84.53984615	-69.69004977	5	77.17876923	-36.75443438
6	81.84330769	-85.490819	6	76.7719230769	-34.98512669
7	82.165	-82.43474207	7	79.43061538	-31.68304977
8	80.84038462	-92.56804977	8	7.254461538461	-31.92904977
9	78.78723077	-73.58820361	9	79.91315385	-40.13220361
10	78.78723077	-97.71512669	10	75.8068461538	-40.45389592
11	80.47138462	-90.79874207	11	78.4655384615	-38.84543438
12	79.02376923	-87.18443438	12	80.63223077	-32.32643438
13	77.09361538	-100.6860498	13	78.21953846	-29.59204977
14	80.03615385	-78.93397284	14	76.05284615	-31.52220361
15	79.71446154	-84.24189592	15	75.57030769	-37.88035746
16	79.30761538	-83.04028053	16	77.737	-32.73328053
17	80.197	-80.62758823	17	76.93276923	-41.49466515
18	82.00415385	-91.60297284	18	78.21953846	-28.06874207
19	77.66130769	-87.42097284	19	76.85707692	-30.55712669
20	81.75815385	-90.63789592	20	76.53538462	-29.59204977

Simulation Inputs Class 2

Particle	X	Y
1	73.15761538	-0.564049766
2	75.892	0.684873311
3	76.61107692	-0.526203612
4	73.71584615	1.167411773
5	75.16346154	1.649950234
6	75.96769231	1.810796388
7	78.62638462	1.006565619
8	78.46553846	0.524027157
9	72.67507692	2.775873311
10	73.47930769	-4.064818996
11	72.83592308	-4.708203612
12	77.57615385	-2.371203612
13	71.62484615	-2.93889592
14	72.26823077	-2.371203612
15	73.47930769	-2.617203612
16	74.19838462	-3.014588227
17	73.64015385	5.756257927
18	71.22746154	4.706027157
19	71.71	3.58010408
20	76.53538462	-1.491280535

Simulation Inputs Class 3

Particle	X	Y
1	81.43646154	49.29825793
2	80.23484615	47.20725793
3	79.98884615	47.45325793
4	80.31053846	53.24371947
5	81.03907692	55.49556562
6	81.75815385	45.04056562
7	79.50630769	45.59879639
8	77.09361538	48.17233485
9	78.05869231	46.56387331
10	78.78723077	46.97071947
11	77.09361538	55.41041177
12	77.66130769	53.08287331
13	82.56238462	48.579181
14	80.79307692	50.50933485
15	71.06661538	51.31356562
16	74.84176923	51.87179639
17	76.85707692	51.38925793
18	78.86292308	49.78079639
19	79.43061538	51.31356562
20	74.68092308	50.424181

Simulation Inputs Class 4

Particle	X	Y
1	79.75230769	91.68595023
2	78.38038462	91.27910408
3	78.78723077	89.75579639
4	79.50630769	89.50979639
5	79.50630769	94.09864254
6	78.46553846	92.72671947
7	78.94807692	95.70710408
8	77.983	94.81771947
9	78.30469231	97.31556562
10	76.61107692	90.399181
11	81.11476923	91.76164254
12	80.23484615	94.17433485
13	77.983	95.86795023
14	76.12853846	97.15471947
15	75.892	95.38541177
16	73.15761538	94.42033485
17	73.23330769	95.30025793
18	74.19838462	96.02879639
19	75.08776923	96.83302716
20	72.99676923	92.1684887

Appendix D: Mean pixel values of the background

	MPVs Background Class 0 Original				MPVs Background Class 0 Simulation			
Particle	ROI1	ROI2	ROI3	ROI4	ROI1	ROI2	ROI3	ROI4
1	549.222	552.889	552.222	550.444	558.778	547.111	548.333	546.556
2	557.111	551.333	556.556	546.333	546.889	544.333	550.444	546.889
3	553.556	561.222	545.889	557.111	549.778	542.778	554.667	544.778
4	556.444	560.667	534.667	556.778	550.556	562.778	551.222	553.889
5	553	547.111	555.111	554.444	556.444	549.667	553.556	547.111
6	549.667	529.333	542.333	551.111	546.111	549.111	541.778	541.889
7	551.444	552	556.778	554.556	550.889	554.556	544.222	559.889
8	549.556	547.111	541.778	540.556	548.778	543.667	541.667	546.333
9	548.889	552	548.889	558.222	556.444	558	553	550.556
10	539.111	537.444	538.222	538.333	541.222	543.889	539.222	537.111
11	545.778	548	541.778	545.778	543.778	546.444	543.667	542.444
12	552.444	552.778	542.889	547.111	547.444	549	551.333	546.556
13	536.889	539	540	540.778	527.222	534.333	540.667	532.889
14	552.556	551.778	554.333	553.778	549.111	548.667	554.778	549.556
15	544.111	555	555	552.111	544.889	541.556	550.111	549.333
16	555.667	552.444	553.556	551.778	549.222	550.778	553.556	554.778
17	552.111	555.667	557.667	558.444	554.333	550.667	554.889	557.222
18	546.222	553.444	547.667	547.556	543.667	542.667	545.889	545
19	552.444	546.333	546.444	548.889	549	547.444	549.111	549.222
20	548.444	553.333	544.333	544	543.889	532.556	545.889	541.444

	MPVs Background Class 1 Original				MPVs Background Class 1 Simulation			
Particle	ROI1	ROI2	ROI3	ROI4	ROI1	ROI2	ROI3	ROI4
1	552.444	550.778	549.333	550.444	549	544.889	552.444	554
2	546.222	556.222	551.889	543.444	550.556	553	560.444	553.333
3	554.889	557	548.222	553.222	557.556	552.333	557.444	553
4	544.444	551.778	554.778	549	562.111	553.333	550.556	552.556
5	551.222	551.556	549	553	559	552.111	556.333	554.778
6	551.889	554.111	556.333	549.333	556.889	554.778	555.667	553.889
7	553.667	545.889	560.667	551.889	558	556	555.556	554.778
8	546.667	558.889	546.111	551.222	551.778	554.556	551.333	548.111
9	552	562	547.778	555.889	554.556	559.444	551.444	558.667
10	558	555	554.444	559	559.889	561.333	553.222	557.111
11	549	557.556	561.333	555.222	556.667	554.111	556.111	559
12	558.778	557.333	555.778	555	554.778	550.333	547.778	552
13	558.111	555.111	549.778	558.667	552.556	552.111	555.778	554
14	559.333	547.333	554.444	552.111	558.222	555	550.556	559.111
15	555.778	564.444	555.667	556.333	553.556	558.667	561.667	558.111
16	543.111	555.444	553	551.444	553.111	552.556	547.111	551.556
17	556.111	549.333	566.222	538.222	551	560.556	554.667	563.778
18	550.778	551.444	554.222	554.222	553.111	552.556	554	550.556
19	550.556	547.333	529.222	559.444	557.333	555.778	551.333	558.778
20	551.444	552.889	547	543.444	559.222	554.667	553.889	547.111

	MPVs Background Class 2 Original				MPVs Background Class 2 Simulation			
Particle	ROI1	ROI2	ROI3	ROI4	ROI1	ROI2	ROI3	ROI4
1	546.667	562.556	553.556	559.889	555.444	563.556	555.333	560.667
2	541	561	554.667	562.778	553	551.222	556.444	551.889
3	554.333	551.667	552.889	554.556	547.778	559.889	554.889	551.222
4	547.222	550.889	561.333	555.667	547.444	565.111	556.222	562.222
5	552.444	557.667	558	554.222	555	559.222	557.222	548.778
6	552.444	552.111	550.222	553.444	561.222	557.111	559	552.667
7	556.444	553.556	553	551.889	560.556	541.111	540.444	552.444
8	555.333	558.556	556.111	549	561.556	555	548.556	550
9	554.778	557.333	550.889	556.667	553.444	566.444	558.444	559.333
10	549.444	559.889	546	555.444	554.556	548.556	550.222	548.111
11	563.333	548.444	555.444	553.333	554.667	552.889	551.778	552.889
12	554	550.222	549.667	540.111	553.667	554.111	545.111	556.333
13	545.667	559.778	557.444	539.333	560	557.222	559.889	550.889
14	543.778	555	554.111	547	554	550.889	556.778	556
15	557.556	550.333	545.222	561.111	555.556	555.778	554.222	554.111
16	552.667	552.667	553.556	554.333	556.333	549.111	560.556	551.333
17	552.444	550.111	546.889	555.778	558.667	555.667	559	557.889
18	553.889	549.222	553.222	558.222	554.778	561.111	555.111	552.778
19	552.222	545.333	548.556	554.333	555.333	553.222	560.222	557
20	555.111	558.778	556.333	551.556	544	558.556	553.222	557.222

	MPVs Background Class 3 Original				MPVs Background Class 3 Simulation			
Particle	ROI1	ROI2	ROI3	ROI4	ROI1	ROI2	ROI3	ROI4
1	553.333	553	549.556	550	555.556	551.889	546.222	550.778
2	548.222	549.444	556.444	553.778	545.667	552.444	554.444	554.667
3	560	541.111	550.556	544.556	554.333	561.222	548.333	552.222
4	560.111	554	554.111	545.222	552.556	559.889	546.556	551.333
5	552.222	561	551.444	553.444	554.333	547.222	559.111	548.556
6	549.222	552.111	556.111	558.889	556.667	551.556	562.778	555.333
7	558.556	555.444	553.111	556.556	551.889	553.889	552.111	554.889
8	556.222	550.667	562.778	559.778	560.444	559	561.333	551.556
9	543.667	555.556	554.444	558.778	549	553.556	561.556	554.556
10	550.444	553.222	563.889	553.444	561.333	555	543.889	553.333
11	557.667	554.556	558.778	558.444	556.778	558.333	558.333	560.333
12	551.111	557.778	564.222	561.778	549	560	557.778	555.444
13	553.222	551	557.667	554	554.111	552.444	558	545.778
14	556.333	545.444	558	556.333	551.333	558.889	559.667	560.778
15	560.556	557.667	565.333	556.333	559.667	562.222	552.222	554.111
16	559.111	556.222	559.222	552.333	561.556	554.111	560	560
17	563.111	557.556	565.111	562.222	553.778	558.667	559.556	565.222
18	555.556	565.667	547.778	547.444	556.889	558.556	552.889	547.778
19	552.889	550.333	550.889	554.556	556.778	549.556	552.778	554.889
20	561.444	559.889	553.667	557.778	563.444	551.222	564.889	556.111

	MPVs Background Class 4 Original				MPVs Background Class 4 Simulation			
Particle	ROI1	ROI2	ROI3	ROI4	ROI1	ROI2	ROI3	ROI4
1	553.889	548.222	549.111	540.111	551.778	549	554.556	548.889
2	539.778	551.667	541.667	557.333	544.222	544.333	551.778	545.889
3	552.667	545.222	548.333	550.889	548	546.778	550.556	548.333
4	549.667	551.333	548	555.333	552.889	545.333	556.556	544.778
5	549.556	548.111	545.444	545.333	550.778	545.333	547.222	549
6	549	547.556	551.556	537.222	546.667	549.222	548.222	545.222
7	536.222	544.444	532.778	542.111	551.889	550.889	544.556	545.667
8	540.111	550.222	549.889	548.333	552.889	545.333	551.889	553.667
9	547.111	541.111	544.333	540	544.778	544.889	543.111	549.667
10	554.778	546.778	552.333	546.111	552.111	547.222	550	552.111
11	545.333	547.111	548	548.667	543.667	549.111	551.333	552.333
12	541.889	542.556	549.667	546.444	545.889	547.556	547.333	548.889
13	540.667	537.333	544.778	544.111	546.222	539.333	547.222	559.778
14	542.111	550.111	550.222	541.222	549.778	552.333	552.556	551.556
15	544.556	551.111	546	548.222	545.444	546.889	543.778	544.667
16	557.667	545	544.556	552.667	555.444	552.556	548.444	550
17	544.444	549.556	549.444	543.556	542.556	553.778	552.556	555
18	541.111	553.889	554.444	548.556	546	553	541.222	538.667
19	548.556	538.333	538.444	552.222	548.667	547.778	546.889	551.778
20	558.556	543.778	550.333	549	555	546.667	555.222	553